

# Probing cosmology and gasphysics with fast radio bursts: Cross-correlations of dark matter haloes and cosmic dispersion measures

Masato Shirasaki<sup>1,2\*</sup>, Ryuichi Takahashi<sup>3</sup>, Ken Osato<sup>4,5</sup>, and Kunihiro Ioka<sup>4</sup>

<sup>1</sup>*National Astronomical Observatory of Japan, Mitaka, Tokyo 181-8588, Japan*

<sup>2</sup>*The Institute of Statistical Mathematics, Tachikawa, Tokyo 190-8562, Japan*

<sup>3</sup>*Faculty of Science and Technology, Hirosaki University, Hirosaki, Aomori 036-8561, Japan*

<sup>4</sup>*Center for Gravitational Physics, Yukawa Institute for Theoretical Physics, Kyoto University, Kyoto 606-8502, Japan*

<sup>5</sup>*LPENS, Département de Physique, École Normale Supérieure, Université PSL, CNRS, Sorbonne Université, Université de Paris, 75005 Paris, France*

YITP-21-80

## ABSTRACT

The column density of free electrons with a cosmological-scale depth, cosmic dispersion measures (DMs), is among the most interesting observables in future transient surveys at radio wavelengths. For future surveys of fast radio bursts (FRBs), we clarify information available from cosmic DMs through cross-correlation analyses of foreground dark matter haloes (hosting galaxies and galaxy clusters) with their known redshifts. With a halo-model approach, we predict that the cross-correlation with cluster-sized haloes is less affected by the details of gasphysics, providing robust cosmological information. For less massive haloes, the cross-correlation at angular scales of  $< 10$  arcmin is sensitive to gas expelled from the halo centre due to galactic feedback. Assuming 20000 FRBs over  $20000 \text{ deg}^2$  with a localisation error being 3 arcmin, we expect that the cross-correlation signal at halo masses of  $10^{12}$ – $10^{14} M_{\odot}$  can be measured with a level of  $\sim 1\%$  precision in a redshift range of  $0 < z < 1$ . Such precise measurements enable to put a 1.5% level constraint on  $\sigma_8 (\Omega_M/0.3)^{0.5}$  and a 3% level constraint on  $(\Omega_b/0.049)(h/0.67)(f_e/0.95)$  ( $\sigma_8$ ,  $\Omega_M$ ,  $\Omega_b$ ,  $h$  and  $f_e$  are the linear mass variance smoothed at  $8 h^{-1} \text{ Mpc}$ , mean mass density, mean baryon density, the present-day Hubble parameter and fraction of free electrons in cosmic baryons today), whereas the gas-to-halo mass relation in galaxies and clusters can be constrained with a level of 10%–20%. Furthermore the cross-correlation analyses can break the degeneracy among  $\Omega_b$ ,  $h$  and  $f_e$ , inherent in the DM-redshift relation.

**Key words:** large-scale structure of Universe – cosmology: theory – fast radio bursts

## 1 INTRODUCTION

Understanding the evolution of cosmic baryons is crucial in modern astronomy. The mean energy density of cosmic baryons has been tightly constrained from measurements of temperature and polarisation fluctuations in the cosmic microwave background (CMB; e.g. Bennett et al. 2013; Planck Collaboration et al. 2020) and primordial deuterium abundance based on big-bang nucleosynthesis (Cooke et al. 2018). Although these probes have provided information about cosmic baryons in the early universe (e.g. Peebles & Yu 1970; Sunyaev & Zeldovich 1970), late-time information is required for a complete understanding of cosmic baryons. The cosmic baryons form large-scale structures through gravitational collapse with dark matter, whereas their cooling and heating processes play an essential role in forming stars and galaxies. Observational estimates have shown that the star formation in galaxies is an inefficient process, even at present, and a large fraction of cosmic baryons would remain in the gaseous phase of the universe (e.g. Fukugita et al. 1998; Fukugita & Peebles 2004). This implies that most baryonic matter in the late-time universe has not been observed, thereby motivating us to develop observational methods to seek the so-called missing baryons.

Most missing baryons are expected to be found in diffuse intergalactic media, which are too faint to detect on an individual basis (see e.g. Bonamente et al. 2016; Nicastro et al. 2018, for recent observational efforts). Various observational probes have been proposed to study baryonic matters less bound to galaxies and stars (e.g. Bregman 2007; McQuinn 2016; Péroux & Howk 2020, for reviews). Among them, we study the dispersion measure (DM), defined as the column density of free electrons in this paper.

The DM has been commonly measured from a frequency-dependent arrival time in radio pulses, allowing us to study electrons in the vicinity of the Milky Way with pulsars so far (e.g. Taylor & Cordes 1993; Crawford et al. 2001; Cordes & Lazio 2002; Yao et al. 2017). New milli-second radio transients located at extragalactic distances, referred to as fast radio bursts (FRBs; Cordes & Chatterjee 2019, for a recent review), have opened a new window for studying the statistical properties of free electrons in an expanding universe (e.g. Ioka 2003; Inoue 2004; Macquart et al. 2020). Ongoing radio transient surveys are aimed at constructing a large sample of FRBs and revealing their origin. They include the Australian Square Kilometre Array Pathfinder (ASKAP<sup>1</sup>) and the Canadian Hydrogen

\* Contact e-mail: [masato.shirasaki@nao.ac.jp](mailto:masato.shirasaki@nao.ac.jp)

<sup>1</sup> <https://www.atnf.csiro.au/projects/askap/index.html>

Intensity Mapping Experiment (CHIME<sup>2</sup>), already providing information about hundreds of FRBs over a sky (e.g. Petroff et al. 2017; The CHIME/FRB Collaboration et al. 2021). Ongoing surveys, such as the Square Kilometre Array (SKA<sup>3</sup>), will further improve the detection rate of FRBs, making  $\sim 10000$  events available in decades (e.g. Connor et al. 2016; Hashimoto et al. 2020).

Because the DM contains all free electrons intervening between a given FRB and us, it is non-trivial how we can learn the redshift evolution of cosmic baryons from DM statistics, even if numerous FRBs become available. To separate the observed DM into several pieces at different redshifts, cross-correlation analyses with galaxies and galaxy clusters have been proposed (e.g. McQuinn 2014; Shirasaki et al. 2017; Madhavacheril et al. 2019; Rafiei-Ravandi et al. 2020). There are two classes of cross-correlations: the angular correlation between the observed DM and spatial positions of galaxies (clusters) (e.g. McQuinn 2014; Shirasaki et al. 2017; Madhavacheril et al. 2019) and the correlation between spatial positions of FRB sources and galaxies (clusters) (e.g. Shirasaki et al. 2017; Rafiei-Ravandi et al. 2020). In this study, we work with the former cross-correlation because it is more sensitive to spatial distributions of electrons in and around gravitational bound objects, referred to as dark matter haloes. Notably, one can extract the information about cosmic free-electron distributions from the latter cross-correlation by dividing FRB sources into subsamples using their DM estimates (Rafiei-Ravandi et al. 2020).

The information contained in cross-correlation has not been explored in detail. McQuinn (2014) showed that cross-correlation can be useful to statistically detect missing baryons around galaxies, whereas cosmological information in the cross-correlation has not been discussed. Shirasaki et al. (2017) proposed cross-correlations as a probe of redshift distributions and host environment of FRBs, but they ignored non-linear effects in the cross-correlation for simplicity. Madhavacheril et al. (2019) focused on using FRBs as a probe of gas densities around galaxies, which is a key quantity in another cosmological observable of the kinematic Sunyaev-Zel'dovich (SZ) effect (Sunyaev & Zeldovich 1980). Rafiei-Ravandi et al. (2020) have shown a realistic forecast of the detectability of FRB-galaxy cross-correlations in ongoing and future surveys, whereas it is still unclear what physics we can learn from a precise measurement of the cross-correlation. Actual analyses with available FRBs and galaxies have already shown a marginal detection of the cross-correlation (Rafiei-Ravandi et al. 2021; Connor & Ravi 2021). Hence, it is timely to study the information content of cross-correlations as probes of missing baryons and cosmology.

In this study, we show that the precise measurement of cross-correlations constrains gas physics and cosmology separately (by breaking the degeneracy). We improve the previous analyses of cross-correlation using a flexible and efficient physical model of cosmic gas density around a given dark matter halo (Aricò et al. 2020) and clarify possible degeneracy between cosmological parameters and assumed baryonic physics. We adopt a halo-model approach (e.g. Cooray & Sheth 2002) to predict cross-correlation and its statistical uncertainty for a given survey configuration. Then, we study the information contents of the cross-correlation in terms of an expected signal-to-noise ratio (SNR) and a forecast of the expected constraints of relevant physical parameters via Fisher analysis. Using the Fisher forecast, we find that cross-correlation allows us to place a tight constraint on cosmological parameters such as the mass variance at linear scales,

the average number density of free electrons in intergalactic media, and gas-to-halo mass relation from galaxy- to cluster-sized haloes.

The rest of this paper is organised as follows. We introduce the observables of interest and the theory of the cross-correlation analysis in Section 2. Next, we describe our model of gas density and the cross-correlation based on the halo model in Section 3. The survey configuration in the Fisher forecast is summarised in Section 4. Section 5 presents the key results, whereas we discuss the limitations of our analysis in Section 6. Finally, concluding remarks are provided in Section 7. In the following,  $\ln$  and  $\log$  represent the natural logarithm and logarithm to base 10, respectively.

## 2 PRELIMINARIES

In this study, we work with an expanding flat geometry universe described using the Friedmann-Robertson-Walker (FRW) metric. Under general relativity, late-time expansion of the universe is governed by the following equation:

$$H(z) = H_0 \sqrt{\Omega_M (1+z)^3 + \Omega_{DE} (1+z)^{3(1+w_0)}}, \quad (1)$$

where  $z$  is the redshift,  $H(z)$  is the Hubble parameter and  $H_0 = 100 h \text{ km/s/Mpc}$  is the present value of  $H(z)$ . In Eq. (1),  $\Omega_M$  and  $\Omega_{DE}$  are the dimensionless density parameter of cosmic matter and dark energy (DE), respectively. It holds that  $\Omega_{DE} = 1 - \Omega_M$  for the flat geometry. We introduce an equation-of-state parameter of DE  $w_0$  and simply assume no redshift dependence of the equation-of-state for DE. Notably,  $w_0 = -1$  sets the DE to a cosmological constant  $\Lambda$ . For a given  $H(z)$ , the radial comoving distance to redshift  $z$  is computed as

$$\chi(z) = \int_0^z \frac{c \, dz'}{H(z')}, \quad (2)$$

where  $c$  is the speed of light. In the following, we will use  $z$  and  $\chi$  interchangeably.

### 2.1 Projected number density field of haloes

Let us assume that we have a sample of haloes distributed over a solid angle of the survey field. The angular number density of haloes per unit steradian can be written as follows:

$$n_h^{2D}(\boldsymbol{\theta}) = \bar{n}_h^{2D} \left[ 1 + \delta_h^{2D}(\boldsymbol{\theta}) \right], \quad (3)$$

where  $\delta_h^{2D}(\boldsymbol{\theta})$  is the projected number density fluctuation field, which is dimension-less.  $\bar{n}_h^{2D}$  is the mean number density, expressed in terms of the halo mass function as follows:

$$\bar{n}_h^{2D} = \int_{\chi_{l,\min}}^{\chi_{l,\max}} d\chi \, \chi^2 \int dM \, \frac{dn}{dM}(M, \chi) S(M, \chi). \quad (4)$$

where  $dn/dM$  is the halo mass function, and  $S(M, \chi)$  is the selection function of halo mass. We introduce a specific form of  $S$  in Subsection 4.1. We here set the range of comoving distances of interest to  $\chi_{l,\min} \leq \chi \leq \chi_{l,\max}$ . The 2D field  $\delta_h^{2D}(\boldsymbol{\theta})$  is expressed in terms of the 3D number density field of haloes as follows:

$$\delta_h^{2D}(\boldsymbol{\theta}) \equiv \frac{1}{\bar{n}_h^{2D}} \int_{\chi_{l,\min}}^{\chi_{l,\max}} d\chi \, \chi^2 \int dM \, \frac{dn}{dM}(M, \chi) S(M, \chi) \times \delta_h(\chi \boldsymbol{\theta}, \chi; M). \quad (5)$$

Here, we introduce the 3D number density fluctuation field of haloes,  $\delta_h$ , via  $n_h(\mathbf{x}; M) = (dn/dM) [1 + \delta_h(\mathbf{x}; M)]$ , where  $n_h(\mathbf{x}; M)$  is the 3D number density field at the position,  $\mathbf{x} = (\chi \boldsymbol{\theta}, \chi)$ , for haloes of mass  $M$ .

<sup>2</sup> <https://chime-experiment.ca/en>

<sup>3</sup> <https://www.skatelescope.org/the-ska-project/>

## 2.2 Dispersion measure field

The DM is defined as the integral of the number density of free electrons along a line-of-sight direction and is observable from the time delay of FRB pulses as varying radio frequencies. In this study, we decompose the observed DM along a given line-of-sight into three components:

$$D_{\text{obs}} = D_{\text{MW}} + D_{\text{LSS}} + D_{\text{source}}, \quad (6)$$

where  $D_{\text{MW}}$  represents contributions from the Milky Way,  $D_{\text{source}}$  represents contributions at the position of the FRB source of interest (basically from the host galaxy, see Subsection 6.3 for details), and  $D_{\text{LSS}}$  includes other contributions from intervening electrons between the source and observer. Notably, LSS means large-scale structures, and  $D_{\text{LSS}}$  comprises circumgalactic, intergalactic and intracluster media. In the following, we pay special attention to  $D_{\text{LSS}}$ , which is expected to be a dominant contribution when the FRB source locates at extra-galactic distance scales.

Considering an FRB at an angular position  $\theta$  on the sky and redshift  $z_s$ , we formally express  $D_{\text{LSS}}$  as

$$D_{\text{LSS}}(\theta, z_s) = \int_0^{\chi_s} d\chi n_e(\chi\theta, \chi) (1 + z(\chi)), \quad (7)$$

where  $\chi_s = \chi(z_s)$ , and  $n_e(\mathbf{x})$  is the comoving number density of free electrons. The average number density of free electrons in intergalactic media is given by (Deng & Zhang 2014)

$$\bar{n}_e(z) = \frac{\bar{\rho}_b}{\mu_e m_p} f_e(z), \quad (8)$$

where  $\bar{\rho}_b$  is the cosmological baryon density in comoving units,  $m_p$  is the proton mass,  $\mu_e = (X_p + Y_p/2)^{-1}$  is the mean molecular weight of electrons,  $X_p$  and  $Y_p$  represent the primordial mass fractions of hydrogen and helium, respectively. In this article, we set  $X_p = 1 - Y_p = 0.76$ . In Eq. (8), we introduce  $f_e(z)$ , which describes the fraction of free electrons in the cosmic electron number density and depends on redshift due to reionisation. At a redshift  $z_s$ ,  $D_{\text{LSS}}$  is expressed as follows:

$$D_{\text{LSS}}(\theta, z_s) = \int_0^{\chi_s} d\chi W_e(\chi) [1 + \delta_e(\chi\theta, \chi)], \quad (9)$$

$$W_e(\chi) \equiv \frac{\bar{\rho}_b}{\mu_e m_p} f_e(z(\chi)) (1 + z(\chi)), \quad (10)$$

where  $\delta_e$  is the 3D number density fluctuation field of free electrons. Eqs. (9) and (10) show that  $D_{\text{LSS}}$  scales with  $\Omega_b h$  where  $\Omega_b$  is the dimensionless baryon density because  $\bar{\rho}_b$  varies with  $\Omega_b h^2$  and the integration in Eq. (9) gives an additional scaling of  $h^{-1}$ .

In reality, an FRB sample would distribute at a wide range of source redshifts. In this case, the DM-field  $D_{\text{LSS}}$  is expressed as follows (Shirasaki et al. 2017):

$$D_{\text{LSS}}(\theta) = \int_0^{\chi_H} d\chi K_e(\chi) [1 + \delta_e(\chi\theta, \chi)], \quad (11)$$

$$K_e(\chi) \equiv W_e(\chi) \int_{\chi}^{\chi_H} d\chi' p(\chi'), \quad (12)$$

where  $\chi_H$  is the comoving distance to  $z \rightarrow \infty$  and  $p(\chi)$  represents the redshift distribution of FRBs. Notably, we reverse the order of integration in  $\chi$  and  $\chi'$  to derive Eq. (11). We adopt the following functional form of  $p(\chi)$ :

$$p(\chi) = p_z(z) \left( \frac{d\chi}{dz} \right)^{-1}, \quad (13)$$

$$p_z(z) = p_0 z^2 \exp(-\alpha z) \Theta(z_{\text{max},f} - z) \Theta(z), \quad (14)$$

where  $\Theta(x)$  is the Heaviside step function,  $\alpha$  and  $z_{\text{max},f}$  are free parameters in the model of  $p(\chi)$ . We assume  $\alpha = 3.5$  and  $z_{\text{max},f} = 5.0$ , which set the median redshift to 0.577. The current observation supports that a major population of FRBs has the source redshift less than unity (The CHIME/FRB Collaboration et al. 2021). Notably, we set the normalisation  $p_0$  in Eq. (14) by imposing  $\int_0^{\infty} dz p_z(z) = 1$ . Our baseline model of the redshift distribution largely corresponds to the scenario of FRBs following the star-formation history (e.g. Muñoz et al. 2016), whereas the realistic values of  $\alpha$  and  $z_{\text{max},f}$  depends on the properties of survey instruments and the origin of FRBs.

## 2.3 Cross-correlations

Our primary focus is to extract the information about cosmic free electrons from cross-correlation analyses between the projected halo density field  $\delta_h^{2D}$  and the DM-field  $D_{\text{obs}}$ . First, we define a two-point cross-correlation function as follows:

$$\xi_{\text{hD}}(\theta) \equiv \langle \delta_h^{2D}(\theta_1) D_{\text{obs}}(\theta_2) \rangle \simeq \langle \delta_h^{2D}(\theta_1) D_{\text{LSS}}(\theta_2) \rangle \quad (15)$$

where  $\langle \dots \rangle$  represents an ensemble average,  $\theta \equiv |\theta_1 - \theta_2|$ , and we assume that there are no correlations among  $\delta_h^{2D}$ ,  $D_{\text{MW}}$  and  $D_{\text{source}}$ . It holds that  $\langle \delta_h^{2D} D_{\text{MW}} \rangle = 0$  because we consider the halo sample at extra-galactic scales. On the other hand, there may exist correlations between  $\delta_h^{2D}$  and  $D_{\text{source}}$  provided some FRBs occur inside the haloes of interest (e.g. Shirasaki et al. 2017). Nevertheless, the correlation of  $\langle \delta_h^{2D} D_{\text{source}} \rangle$  is largely uncertain at present because it is related to the origin of FRBs. Notably,  $D_{\text{source}}$  has been estimated to be  $\lesssim 200 \text{ pc/cm}^3$  for FRB host galaxies with known redshifts, except for FRB 190520 (e.g. Spitler et al. 2016; Chatterjee et al. 2017; Tendulkar et al. 2017; Kokubo et al. 2017; Basso et al. 2017; Prochaska et al. 2019; Ravi et al. 2019; Bannister et al. 2019; CHIME/FRB Collaboration et al. 2020; Chittidi et al. 2020; Bhandari et al. 2020a,b; Mannings et al. 2020; Marcote et al. 2020; Macquart et al. 2020; Simha et al. 2020; Law et al. 2020; Heintz et al. 2020; James et al. 2021; Bhardwaj et al. 2021). Hence, we simply ignore the term of  $\langle \delta_h^{2D} D_{\text{source}} \rangle$  in the cross-correlation function. We briefly discuss the impact of  $\langle \delta_h^{2D} D_{\text{source}} \rangle$  on our analysis in Subsection 6.3, whereas we leave the investigation of  $\langle \delta_h^{2D} D_{\text{source}} \rangle$  for future studies.

The cross-correlation in Fourier space is called the cross power spectrum<sup>4</sup>, which is defined as follows:

$$\langle \tilde{\delta}_h^{2D}(\ell_1) \tilde{D}_{\text{LSS}}(\ell_2) \rangle \equiv (2\pi)^2 \delta_D^{(2)}(\ell_1 + \ell_2) C_{\text{hD}}(\ell_1), \quad (16)$$

where  $C_{\text{hD}}$  is the cross power spectrum,  $\delta_D^{(n)}(\mathbf{x})$  is the  $n$ -dimensional Dirac delta function,  $\tilde{\delta}_h^{2D}$  is the Fourier transform of  $\delta_h^{2D}$  and so on. The cross power spectrum is equivalent to the Fourier transform of  $\xi_{\text{hD}}$ , and it holds that

$$\xi_{\text{hD}}(\theta) = \int \frac{d^2\ell}{(2\pi)^2} C_{\text{hD}}(\ell) \exp(i\ell \cdot \theta). \quad (17)$$

Then, we relate the two-point correlation function  $\xi_{\text{hD}}$  with clustering information of underlying 3D fields  $\delta_h(\mathbf{x}, M)$  and  $\delta_e(\mathbf{x})$ . Using

<sup>4</sup> In this paper, we work with a flat-sky approximation. The power spectrum is defined in Fourier space throughout our paper. Hence, a multipole  $\ell$  consists of real numbers. In Eq. (17), the norm of multipole  $\ell = |\ell|$  is loosely related to an angular separation  $\theta$  by  $\ell = 1/\theta \approx 3437 (\theta/1 \text{ arcmin})^{-1}$ .

Eqs. (5) and (11), we obtain

$$\begin{aligned} \xi_{\text{hD}}(\theta) &= \frac{1}{\bar{n}_{\text{h}}^{2\text{D}}} \int_{\chi_{\text{l},\text{min}}}^{\chi_{\text{l},\text{max}}} d\chi_1 \chi_1^2 \int_0^{\chi_{\text{H}}} d\chi_2 K_{\text{e}}(\chi_2) \\ &\times \int dM \frac{dn}{dM}(M, \chi_1) S(M, \chi_1) \int \frac{d^3k}{(2\pi)^3} P_{\text{he}}(k, M, \chi_1, \chi_2) \\ &\times \exp[i\mathbf{k}_{\perp} \cdot (\chi_1 \boldsymbol{\theta}_1 - \chi_2 \boldsymbol{\theta}_2)] \exp[ik_{\parallel} (\chi_1 - \chi_2)], \end{aligned} \quad (18)$$

where  $\mathbf{k} = (\mathbf{k}_{\perp}, k_{\parallel})$ , we perform the Fourier transform of the 3D fields of  $\delta_{\text{h}}$  and  $\delta_{\text{e}}$ , and define the 3D power spectrum as

$$\langle \tilde{\delta}_{\text{h}}(\mathbf{k}_1, M, \chi_1) \tilde{\delta}_{\text{e}}(\mathbf{k}_2, \chi_2) \rangle \equiv (2\pi)^3 \delta_{\text{D}}^{(3)}(\mathbf{k}_1 + \mathbf{k}_2) P_{\text{he}}(k_1, M, \chi_1, \chi_2). \quad (19)$$

We adopt the Limber approximation (Limber 1954) so that

$$\begin{aligned} &\int \frac{dk_{\parallel}}{2\pi} P_{\text{he}}(k, M, \chi_1, \chi_2) \exp[ik_{\parallel} (\chi_1 - \chi_2)] \\ &\simeq P_{\text{he}}(k_{\perp}, M, \chi_1, \chi_2) \delta_{\text{D}}^{(1)}(\chi_1 - \chi_2). \end{aligned} \quad (20)$$

Using Eq. (17), we obtain

$$\begin{aligned} C_{\text{hD}}(\ell) &= \frac{1}{\bar{n}_{\text{h}}^{2\text{D}}} \int_{\chi_{\text{l},\text{min}}}^{\chi_{\text{l},\text{max}}} d\chi K_{\text{e}}(\chi) \int dM \frac{dn}{dM}(M, \chi) S(M, \chi) \\ &\times P_{\text{he}}\left(k = \frac{\ell}{\chi}, M, \chi, \chi\right), \end{aligned} \quad (21)$$

where we use  $\mathbf{k}_{\perp} \chi = \ell$  to derive Eq. (21). In the following, we study the cross power spectrum  $C_{\text{hD}}$  to extract the clustering information of cosmic free electrons around a given sample of haloes and cosmological parameters. For a simpler notation, we write  $P_{\text{he}}(k = \ell/\chi, M, \chi, \chi)$  as  $P_{\text{he}}(k = \ell/\chi, M, \chi)$  below.

### 3 MODEL OF FREE ELECTRONS

#### 3.1 Halo model

To compute the cross power spectrum  $C_{\text{hD}}$ , we need the model of the 3D power spectrum of  $P_{\text{he}}$  defined in Eq. (19). We adopt a halo-model approach (Cooray & Sheth 2002; Rafiei-Ravandi et al. 2020) to compute  $P_{\text{he}}$ .

The halo model assumes that all free electrons are associated with single haloes. Under this assumption, the power spectrum can be decomposed into two parts:

$$P_{\text{he}}(k, M, z) = P_{\text{he}}^{1\text{h}}(k, M, z) + P_{\text{he}}^{2\text{h}}(k, M, z), \quad (22)$$

where  $z$  is the redshift corresponding to a given comoving distance  $\chi$ . The former and latter on the right-hand side in Eq. (22) are 1- and 2-halo terms, respectively. The 1-halo term arises from the two-point correlation in single haloes, whereas the 2-halo term expresses the two-point correlation function between neighbouring haloes. Considering that free electrons around a halo of  $M$  follow a spherical density profile of  $n_{\text{e,h}}(r, M, z)$ , we obtain

$$P_{\text{he}}^{1\text{h}}(k, M, z) = \frac{\tilde{n}_{\text{e,h}}(k, M, z)}{\bar{n}_{\text{e,hm}}(z)}, \quad (23)$$

$$\begin{aligned} P_{\text{he}}^{2\text{h}}(k, M, z) &= \int dM' \frac{dn}{dM'}(M', z) \frac{\tilde{n}_{\text{e,h}}(k, M', z)}{\bar{n}_{\text{e,hm}}(z)} \\ &\times P_{\text{hh}}(k, M, M', z), \end{aligned} \quad (24)$$

$$\bar{n}_{\text{e,hm}}(z) = \int dM \frac{dn}{dM}(M, z) \int dV n_{\text{e,h}}(r, M, z), \quad (25)$$

where  $\tilde{n}_{\text{e,h}}$  is the Fourier transform of the density profile

$n_{\text{e,h}}(r, M, z)$ , and  $P_{\text{hh}}(k, M, M', z)$  is the 3D power spectrum between  $\delta_{\text{h}}(\mathbf{x}, M)$  and  $\delta_{\text{h}}(\mathbf{x}, M')$  at redshift  $z$ . We adopt the linear approximation for  $P_{\text{hh}}(k, M, M', z)$ :

$$P_{\text{hh}}(k, M, M', z) \simeq b_{\text{h}}(M, z) b_{\text{h}}(M', z) P_{\text{L}}(k, z), \quad (26)$$

where  $b_{\text{h}}$  is the linear halo bias, and  $P_{\text{L}}$  represents the linear matter power spectrum.

To specify our halo model, we set the halo mass of  $M$  by a spherical overdensity mass at 200 times the critical density, referred to as  $M_{200\text{c}}$  in the literature. For this mass, we adopt the model of the halo mass function in Tinker et al. (2008) and the linear halo bias in Tinker et al. (2010). In addition, we compute the linear matter power spectrum using a Boltzmann code (CAMB, see Lewis et al. 2000, for details). The key ingredient of our model,  $n_{\text{e,h}}$ , is set in the next subsection.

#### 3.2 Two-component gas model

For the number density profile of electrons around a halo, we adopt the model developed in Schneider & Teyssier (2015); Aricò et al. (2020). The model assumes that gas in a given halo of  $M$  comprises two components: a hot gas, assumed to be in hydrostatic equilibrium inside haloes, and a gas ejected from the halo due to some feedback processes by, e.g. active galactic nuclei (AGN).

We consider four free parameters for the gas model: a typical distance scale of ejected gas from the halo centre ( $\eta$ ), a characteristic halo mass for which 50% of the gas in a halo is in the hot bound state ( $M_{\text{c}}$ ), mass dependence of the gas depletion by the feedback ( $\beta$ ), and a characteristic halo mass providing the stellar mass fraction of 0.023 at  $z = 0$  ( $M_{1,0}$ ). Aricò et al. (2020) calibrated these parameters with a set of hydrodynamical simulations so that the model can reproduce the power spectrum of the matter density fields in the simulations. Notably, direct calibrations of gas density profiles were not performed in Aricò et al. (2020).

Hence, the model is still phenomenological and not accurate enough for some purposes (e.g. the application to real data in the future). Nevertheless, we find that the halo-model prediction with the gas model in Aricò et al. (2020) can explain cross power spectra based on the TNG simulation (Springel et al. 2018) within a level of  $\sim 25\%$ – $30\%$  at a wide range of halo masses, redshifts and multipoles  $\ell$  (also see Appendix B). We believe that our model is sufficient to study information contents in the cross power spectra of  $C_{\text{hD}}$  at this early stage. We leave more careful modelling of  $C_{\text{hD}}$  for future studies.

Table 1 lists our model parameters and the inferred values from the analysis in Aricò et al. (2020) for different hydrodynamical simulations.

Apart from the parameters for gas density, we also introduce two nuisance parameters to marginalise over uncertainties in baryonic effects in total matter density profiles in single haloes ( $A_{\text{DK15}}$  in Eq. [28]) and the amplitude in the fraction of free electrons in cosmic baryon density ( $A_{\text{e,norm}}$  in Eq. [36]).

##### 3.2.1 Bound gas

For the hot gas component, the mass density profile is modelled as

$$\rho_{\text{BG}}(r) = f_{\text{BG}} M \begin{cases} y_0 [x^{-1} \ln(1+x)]^{\Gamma} & r < r_{200\text{c}}/\sqrt{5} \\ y_1 x^{-1} (1+x)^{-2} & r_{200\text{c}}/\sqrt{5} \leq r < r_{200\text{c}} \\ 0 & r \geq r_{200\text{c}} \end{cases}, \quad (27)$$

**Table 1.** A short summary of the model parameters of stars and gas in Aricò et al. (2020). The parameter  $\eta$  is a typical distance scale of a gas particle expelled by the feedback (in units of  $5.30 r_{200c}$ ),  $M_c$  gives the halo mass for which 50% of the gas in haloes is in the hot and bound state,  $\beta$  controls how rapidly the gas mass in the hot state decreases as reducing the halo mass, and  $M_{1,0}$  is the pivot halo mass giving the mass fraction of stars being 0.023 at  $z = 0$ . We list the inferred value of each parameter in Aricò et al. (2020) for different hydrodynamical simulations: TNG300 (Springel et al. 2018), BAHAMAS (McCarthy et al. 2017), Cosmo-OWLS (Le Brun et al. 2014), Horizon-AGN (Dubois et al. 2014) and EAGLE (Schaye et al. 2015; Hellwing et al. 2016). Note that we adopt the best-fit parameters of  $\eta$ ,  $M_c$  and  $\beta$  for the simulations at  $z = 0$  and ignore a mild redshift dependence throughout the paper.

Parameters	TNG300	BAHAMAS	Cosmo-OWLS	Horizon-AGN	EAGLE
$\eta$	0.14	0.53	0.35	0.15	0.14
$M_c$ [ $10^{13} h^{-1} M_\odot$ ]	2.3	3.8	0.4	1.2	1.8
$\beta$	4.09	0.47	0.25	6.38	9.65
$M_{1,0}$ [ $10^{11} h^{-1} M_\odot$ ]	0.22	10.85	1.61	0.07	11.15

where  $r_{200c}$  is given by  $r_{200c} = (1+z) [3M/(4\pi\rho_{\text{crit}}(z))/200]^{1/3}$  and  $\rho_{\text{crit}}(z) = 3H^2(z)/(8\pi G)$  is the critical density in the universe at redshift  $z$ ,  $x = r/r_s$  and  $r_s$  is the scale radius of a spherical Navarro-Frenk-White (NFW) profile for dark matter haloes (Navarro et al. 1996). Notably, we work with the comoving coordinate. To compute the scale radius, we introduce a halo concentration parameter as  $c_h = r_{200c}/r_s$ . We adopt the model of  $c_h$  in Diemer & Kravtsov (2015) with a free normalisation, i.e.

$$c_h(M, z) = A_{\text{DK15}} c_{\text{DK15}}(M, z), \quad (28)$$

where  $A_{\text{DK15}}$  is a free parameter and  $c_{\text{DK15}}$  is the model in Diemer & Kravtsov (2015). Notably,  $c_{\text{DK15}}$  depends on the amplitude and shape of the linear matter power spectrum  $P_L$  (see Diemer & Kravtsov 2015, for details). Hence, the concentration shows a cosmological dependence; it is also affected by baryonic feedback processes in single halos (e.g. Duffy et al. 2010). Thus, we include the free parameter  $A_{\text{DK15}}$  to marginalise the baryonic effects in  $c_h$ . The inner slope of  $\Gamma$  in Eq. (27) is defined such that the hydrostatic gas has the same slope of the NFW at  $r = r_{200c}/\sqrt{5}$ . To be specific, it is given by

$$\Gamma(M, z) = \frac{(1 + 3c_h/\sqrt{5}) \ln(1 + c_h/\sqrt{5})}{(1 + c_h/\sqrt{5}) \ln(1 + c_h/\sqrt{5}) - c_h/\sqrt{5}}. \quad (29)$$

The normalisation factors  $y_0$  and  $y_1$  are set so that the profile can be continuous and  $\int 4\pi r^2 dr \rho_{\text{BG}}(r) = f_{\text{BG}} M$ . We assume that the gas fraction  $f_{\text{BG}}$  depends on the mass  $M$  and redshifts  $z$ :

$$f_{\text{BG}}(M, z) = \frac{\Omega_b/\Omega_M - f_{\text{star}}(M, z)}{1 + (M_c/M)^\beta}, \quad (30)$$

where  $f_{\text{star}}$  describes the stellar-to-halo mass ratio,  $M_c$  and  $\beta$  are free parameters in the model. The explicit form of  $f_{\text{star}}$  is given in Appendix A; it contains a single free parameter  $M_{1,0}$  giving  $f_{\text{star}} = 0.023$  at  $M = M_{1,0}$  and  $z = 0$ .

### 3.2.2 Ejected gas

The gas ejected from the halo is assumed to follow the density distribution below:

$$\rho_{\text{EG}}(r) = \frac{f_{\text{EG}} M}{(2\pi r_{\text{ej}}^2)^{3/2}} \exp\left[-\frac{1}{2} \left(\frac{r}{r_{\text{ej}}}\right)^2\right], \quad (31)$$

where the profile is derived via a Maxwell-Boltzmann velocity distribution of the particles expelled by the AGN under simple circumstances (Schneider & Teyssier 2015). The radius  $r_{\text{ej}}$  is a parameter in the model. For convenience, we introduce a dimensionless parameter for  $r_{\text{ej}}$ :

$$r_{\text{ej}} = 0.75 \eta r_{\text{esc}}, \quad (32)$$

where  $\eta$  is the model parameter and  $r_{\text{esc}}$  is the halo escape radius. We estimate  $r_{\text{esc}}$  by the distance travelled by a gas particle with a constant halo escape velocity over a time-scale of a half Hubble time. For the mass of  $M$ ,  $r_{\text{esc}}$  is given by  $7.07 r_{200c}$ . The mass fraction of ejected gas is simply set as follows:

$$f_{\text{EG}}(M, z) = \Omega_b/\Omega_M - f_{\text{BG}}(M, z) - f_{\text{star}}(M, z). \quad (33)$$

### 3.2.3 Conversion of gas to electron

For given density profiles of  $\rho_{\text{BG}}$  and  $\rho_{\text{EG}}$ , we convert the gas mass density into the number density of electrons with a constant factor:

$$n_{\text{e,h}}(r, M, z) = \frac{\rho_{\text{BG}}(r, M, z) + \rho_{\text{EG}}(r, M, z)}{\mu'_e(z) m_p}, \quad (34)$$

where  $\mu'_e(z)$  is an effective molecular weight of electrons at different  $z$ . We simply set  $\mu'_e(z) = (X_p + Y_p/2)^{-1}$ . Notably, our results are insensitive to the choice of  $\mu'_e(z)$  because the normalisation is cancelled in the halo model (see Eqs. [23]-[25]).

## 3.3 Fraction of free electrons in cosmic baryons

The overall amplitude of  $C_{\text{hD}}$  depends on the fraction of free electrons in baryon density,  $f_e$  in Eq. (8). At high redshifts ( $z \gtrsim 6$ ), the gas is expected to still be neutral. At lower redshifts, the fraction of free electrons would rapidly grow because of hydrogen reionisation and increases further at the epoch of helium reionisation. Even after the helium reionisation, the fraction can decrease because some fraction of the electrons may be confined in stars and black holes.

We use a realistic model of  $f_e(z)$ , which has been calibrated in Takahashi et al. (2021). The model is given by

$$f_{e,\text{T21}}(z) = 0.475(z + 0.703)^{0.02} [1 - \tanh\{3.19(z - 5.42)\}], \quad (35)$$

where it can reproduce the fraction of free electrons in the TNG simulation. To make our halo model self-consistent, we include the possible dependence of  $f_e$  on gas-to-star conversion and possible uncertainties in Eq. (35). Our final model of  $f_e(z)$  is then given by

$$f_e(z) = A_{\text{e,norm}} f_{e,\text{T21}}(z) \frac{\rho_{\text{tot,gas}}(z; M_{1,0})}{\rho_{\text{tot,gas}}(z; M_{1,0})|_{\text{TNG}}}, \quad (36)$$

where  $A_{\text{e,norm}}$  is a free parameter in the model, and we define

$$\rho_{\text{tot,gas}}(z; M_{1,0}) = \int dM \frac{dn}{dM}(M, z) M \left[ \frac{\Omega_b}{\Omega_M} - f_{\text{star}}(M, z) \right], \quad (37)$$

and  $\rho_{\text{tot,gas}}|_{\text{TNG}}$  represents the result when we set  $M_{1,0} = 2.2 \times 10^{10} h^{-1} M_\odot$ .

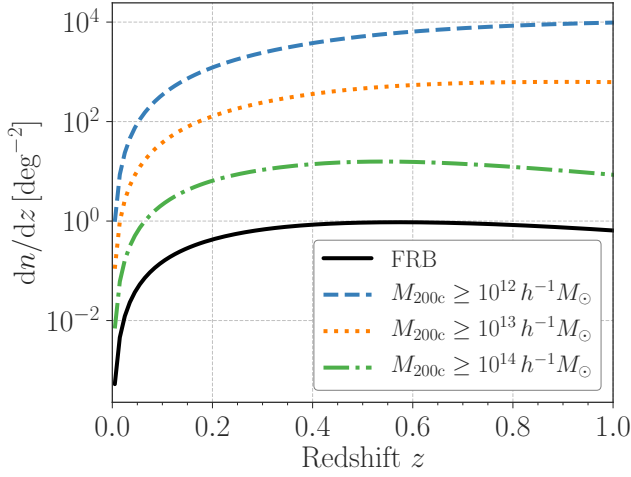


**Figure 1.** The redshift distribution of FRBs and foreground haloes in our fiducial analysis setup.

#### 4 ANALYSIS SETUP

In this section, we summarise the setup for cross-correlation analyses in an FRB hypothetical survey. We assume that halo/FRB catalogues covering a sky of  $20000 \text{ deg}^2$  are available. This sky coverage is close to the one proposed in upcoming galaxy surveys by The ten-year Rubin Observatory Legacy Survey of Space and Time (LSST)<sup>5</sup> and *Euclid*<sup>6</sup>.

##### 4.1 Foreground haloes

We consider an ideal setup of foreground halo samples to give some sense of how much information contents can be extracted from cross-correlation analyses. For cross-correlations, we study three mass-limited samples with  $M \geq M_{\text{thre}}$  at five redshift bins. As a representative example, we use three mass thresholds of  $M_{\text{thre}} [h^{-1} M_{\odot}] = 10^{12}, 10^{13}$  and  $10^{14}$ . The halo masses of  $10^{12}, 10^{13}$  and  $10^{14} h^{-1} M_{\odot}$  largely correspond to the galaxy main sequence, red luminous galaxies and galaxy clusters, respectively (Wechsler & Tinker 2018). We further assume that the halo catalogue contains no satellite galaxies for simplicity. In this setup, the mass selection function  $S(M)$  is simply given by  $S(M) = \Theta(M - M_{\text{thre}})$ . For the redshift bins, we set the edge of each bin to  $0 < z \leq 0.2$ ,  $0.2 < z \leq 0.4$ ,  $0.4 < z \leq 0.6$ ,  $0.6 < z \leq 0.8$  and  $0.8 < z \leq 1.0$ . We assume that the redshifts of individual haloes are precisely measured and do not consider any errors in their redshift measurements. A more realistic model of galaxies and clusters based on, e.g. halo occupation distribution (e.g. Berlind et al. 2003) would be relevant to actual analyses, but we leave it for future studies. Figure 1 shows the redshift distribution of the foreground halo samples and FRBs.

##### 4.2 Properties of FRBs

For the cross-correlation analysis, we have to set the average angular number density of FRBs  $\bar{n}_{\text{FRB}}$ , the variance of DM associated with FRB host galaxies, denoted as  $\sigma_{\text{DM}}$ , and the angular resolution of

FRB position's  $\Delta\theta_{\text{FRB}}$ . We assume that  $D_{\text{MW}}$  can be precisely subtracted from the observed DM and ignore possible small variance from the residual of  $D_{\text{MW}}$ . We also assume that the redshift distribution FRBs is given by Eq. (14). For a given  $\Delta\theta_{\text{FRB}}$ , we compute a smearing effect on the cross power spectrum due to the uncertainty of the FRB locations as follows (Rafiei-Ravandi et al. 2020):

$$C_{\text{hD}}(\ell) \rightarrow C_{\text{hD}}(\ell) \mathcal{B}(\ell), \quad (38)$$

$$\mathcal{B}(\ell) = \exp\left(-\frac{(\Delta\theta_{\text{FRB}}\ell)^2}{16 \ln 2}\right), \quad (39)$$

where  $\Delta\theta_{\text{FRB}}$  provides a full width at half maximum in the Gaussian probability distribution of angular positions for individual FRBs.

For our fiducial case, we set  $\bar{n}_{\text{FRB}} = 1 \text{ deg}^{-2}$ ,  $\sigma_{\text{DM}} = 60 \text{ pc/cm}^3$ , and  $\Delta\theta_{\text{FRB}} = 3 \text{ arcmin}$ . We set the value of  $\sigma_{\text{DM}} = 60 \text{ pc/cm}^3$  following the estimate of the probability distribution of  $D_{\text{source}}$  in Macquart et al. (2020). Our fiducial values of  $\bar{n}_{\text{FRB}} = 1 \text{ deg}^{-2}$  and  $\Delta\theta_{\text{FRB}} = 3 \text{ arcmin}$  can be realised in future FRB surveys (e.g. CHIME/FRB Collaboration et al. 2018), whereas we will examine two other cases of  $(\bar{n}_{\text{FRB}}, \Delta\theta_{\text{FRB}}) = (0.1 \text{ deg}^{-2}, 1 \text{ arcmin})$  and  $(10 \text{ deg}^{-2}, 10 \text{ arcmin})$  as required.

##### 4.3 Statistical errors

To compute the statistical error, we assume that the relevant random fields of  $\delta_{\text{h}}^{2\text{D}}$  and  $D_{\text{obs}}$  follow Gaussian statistics. When we measure the cross power spectrum at bins of multipole  $\ell$  with a bin width being  $\Delta\ell$ , the covariance matrix of two power spectra is expressed as follows:

$$\begin{aligned} & \text{Cov} [C_{\text{hD}}(\ell_i, z_{\mu}, M_{\text{thre},p}), C_{\text{hD}}(\ell_j, z_{\nu}, M_{\text{thre},q})] \\ &= \frac{\delta_{ij}^{\text{K}}}{f_{\text{sky}} 2\ell_i \Delta\ell} \left[ \delta_{\mu\nu}^{\text{K}} C_{\text{DD}}(\ell_i) C_{\text{hh}}(\ell_i; z_{\mu}, M_{\text{thre},p}, M_{\text{thre},q}) \right. \\ & \quad \left. + C_{\text{hD}}(\ell_i, z_{\mu}, M_{\text{thre},p}) C_{\text{hD}}(\ell_i, z_{\nu}, M_{\text{thre},q}) \right], \quad (40) \end{aligned}$$

where  $C_{\text{hD}}(\ell_i, z_{\mu}, M_{\text{thre},p})$  is the cross power spectrum at  $\ell = \ell_i$  for haloes with  $M \geq M_{\text{thre},p}$  at the  $\mu$ -th redshift bin,  $C_{\text{DD}}$  is the auto power spectrum of  $D_{\text{obs}}$ ,  $C_{\text{hh}}(\ell; z_{\mu}, M_{\text{thre},p}, M_{\text{thre},q})$  represents the power spectrum between two halo samples of  $M \geq M_{\text{thre},p}$  and  $M \geq M_{\text{thre},q}$  at the  $\mu$ -th redshift bin,  $f_{\text{sky}}$  is the fraction of the sky coverage, and  $\delta_{ij}^{\text{K}}$  is the Kronecker delta symbol.

Using the Limber approximation, we write the auto power spectrum of  $D_{\text{obs}}$  as follows:

$$C_{\text{DD}}(\ell) \simeq C_{\text{DD,IGM}}(\ell) \mathcal{B}^2(\ell) + \frac{\sigma_{\text{DM}}^2}{\bar{n}_{\text{FRB}}}, \quad (41)$$

$$C_{\text{DD,IGM}}(\ell) = \int_0^{\chi_{\text{H}}} d\chi \frac{K_{\text{e}}^2(\chi)}{\chi^2} P_{\text{e}}\left(\frac{\ell}{\chi}, z(\chi)\right), \quad (42)$$

where  $P_{\text{e}}(k, z)$  is the 3D auto power spectrum of  $\delta_{\text{e}}(\mathbf{x})$ . We adopt the fitting formula of  $P_{\text{e}}(k, z)$  in Takahashi et al. (2021). Note that we ignore contributions from the clustering of sources in Eq. (41), but they are expected to be sub-dominant (e.g. Shirasaki et al. 2017). Similarly, the power spectrum of  $C_{\text{hh}}$  is expressed as follows:

$$C_{\text{hh}}(\ell; z_{\mu}, M_{\text{thre},p}, M_{\text{thre},q}) = C_{\text{hh,cl}}(\ell; \mu, p, q) + \frac{\delta_{pq}^{\text{K}}}{\bar{n}_{\text{h},\mu p}^2}, \quad (43)$$

$$\begin{aligned} C_{\text{hh,cl}}(\ell; \mu, p, q) &= \int_{\chi_{\text{min},\mu}}^{\chi_{\text{max},\mu}} d\chi \chi^2 P_{\text{L}}\left(\frac{\ell}{\chi}, z(\chi)\right) \\ & \quad \times b_{\text{S},\mu p}(z(\chi)) b_{\text{S},\mu q}(z(\chi)) \quad (44) \end{aligned}$$

<sup>5</sup> <https://www.lsst.org/>

<sup>6</sup> <https://www.euclid-ec.org/>

where  $\chi_{\min,\mu}$  and  $\chi_{\max,\mu}$  set the boundary in the range of comoving distances at the  $\mu$ -th redshift bin, and

$$\bar{n}_{h,\mu\text{p}}^{2\text{D}} = \int_{\chi_{\min,\mu}}^{\chi_{\max,\mu}} d\chi \chi^2 \int dM \frac{dn}{dM}(M, \chi) S_{\text{p}}(M), \quad (45)$$

$$b_{S,\mu\text{p}}(z) = \frac{1}{\bar{n}_{h,\mu\text{p}}^{2\text{D}}} \int dM \frac{dn}{dM}(M, z) S_{\text{p}}(M) b_{\text{h}}(M, z), \quad (46)$$

$$S_{\text{p}}(M) \equiv \Theta(M - M_{\text{thre},p}). \quad (47)$$

#### 4.4 Fisher matrix

To quantify information contents in  $C_{\text{hD}}$ , we measure the constraining power of some physical parameters based on a Fisher formalism. Suppose that we measure the cross power spectra  $C_{\text{hD}}$  for three mass-limited halo catalogues at five redshift bins. Then, we construct the data vector of  $\mathbf{D}$  as follows:

$$\begin{aligned} \mathbf{C}_{\mu,p} &= \{C_{\text{hD}}(\ell_1, z_{\mu}, M_{\text{thre},p}), C_{\text{hD}}(\ell_2, z_{\mu}, M_{\text{thre},p}), \\ &\quad \dots, C_{\text{hD}}(\ell_N, z_{\mu}, M_{\text{thre},p})\} \quad (48) \\ \mathbf{D} &= \{\mathbf{C}_{1,1}, \mathbf{C}_{1,2}, \mathbf{C}_{1,3}, \mathbf{C}_{2,1}, \mathbf{C}_{2,2}, \mathbf{C}_{2,3}, \\ &\quad \dots, \mathbf{C}_{5,1}, \mathbf{C}_{5,2}, \mathbf{C}_{5,3}\}, \quad (49) \end{aligned}$$

where we set the number of  $\ell$  bins to  $N$ , and the data vector comprises  $N \times 3 \times 5$  power spectra. We perform a logarithmic binning in a range of  $10 < \ell < \ell_{\text{max}}$  with the logarithmic bin width being  $\Delta \ln \ell = 0.4$ . We will examine two cases of  $\ell_{\text{max}} = 3000$  and  $10000$ . We consider the Fisher analysis with  $\ell_{\text{max}} = 3000$  as our baseline, whereas the results with  $\ell_{\text{max}} = 10000$  can give some sense of how much information remains at sub-arcmin scales.

For physical parameters of interest  $s$ , the Fisher matrix is then defined as follows:

$$\begin{aligned} F_{ij} &= \sum_{\alpha,\beta} \frac{\partial D_{\alpha}}{\partial s_i} \text{Cov}_{\alpha\beta}^{-1} \frac{\partial D_{\beta}}{\partial s_j} \\ &+ \frac{1}{2} \sum_{\alpha,\beta,\gamma,\delta} \text{Cov}_{\alpha\beta}^{-1} \frac{\partial \text{Cov}_{\beta\gamma}}{\partial s_i} \text{Cov}_{\gamma\delta}^{-1} \frac{\partial \text{Cov}_{\delta\alpha}}{\partial s_j}, \quad (50) \end{aligned}$$

where Cov is the covariance matrix for the data vector  $\mathbf{D}$ , which is given by Eq. (40). Throughout this paper, we ignore the second term in the right-hand side of Eq. (50) because the covariance scales with the inverse of the survey area, and it is expected to be subdominant for the analysis with  $20000 \text{ deg}^2$ . When  $\Delta s_i$  represents the statistical error in the parameter of  $s_i$  inferred from a measurement of  $\mathbf{D}$ , the inverse of the Fisher matrix  $F_{ij}^{-1}$  provides an estimate of the correlation between  $\Delta s_i$  and  $\Delta s_j$ .

In our setup, we have six parameters to compute the linear matter power spectrum  $P_{\text{L}}(k, z)$  and the property of dark matter haloes: the dimensionless Hubble parameter  $h$ , equation-of-state parameter of the DE  $w_0$ , matter density  $\Omega_{\text{M}}$ , baryon density  $\Omega_{\text{b}}$ , spectral index of primordial power spectrum  $n_s$  and linear mass variance smoothed with the scale of  $8 h^{-1} \text{ Mpc}$  at  $z = 0$ ,  $\sigma_8$ .

In addition, there are four parameters to determine the gas properties around dark matter haloes, referred to as  $\eta$ ,  $M_c$ ,  $\beta$  and  $M_{1,0}$  (see Table 1 and Subsection 3.2 for details) and two nuisance parameters of  $A_{\text{DK15}}$  and  $A_{\text{e,norm}}$ . To make our analysis realistic as possible, we allow the mass thresholds of  $M_{\text{thre}} = 10^{12}$ ,  $10^{13}$  and  $10^{14} h^{-1} M_{\odot}$  and the parameter of the FRB redshift distribution (i.e.  $\alpha$  in Eq. [14]) to vary.

Therefore, we have  $6 + 4 + 2 + 4 = 16$  free parameters in the model of our data vector  $\mathbf{D}$ . Owing to the strong degeneracy among parameters in the power spectra, we need to introduce loose priors

**Table 2.** The list of parameters in our Fisher analysis. Assuming three different mass-limited samples, we have 16 parameters in total, consisting of 6 cosmological parameters, 4 astrophysical parameters (see Table 1 for details), 2 nuisance parameters in the halo concentration (Eq. [28]) and  $f_{\text{e}}$  (Eq. [36]), 3 thresholds of the mass-limited samples, and 1 for the FRB redshift distribution (see Eq. [14]). Note that the parameters of  $M_c$ ,  $M_{1,0}$  and  $M_{\text{thre},i}$  ( $i = 1, 2, 3$ ) are in units of  $h^{-1} M_{\odot}$ . For the fiducial astrophysical parameters, we use the values relevant to the TNG simulation.

Parameters	Fiducial	Gaussian prior $\sigma_{\text{prior},i}$
Cosmology		
$h$	0.673	0.1
$w_0$	-1	0.2
$\Omega_{\text{M}}$	0.315	0.10
$\Omega_{\text{b}}$	0.0491	0.020
$\sigma_8$	0.831	0.1
$n_s$	0.965	0.1
Astrophysics (Gas)		
$\log \eta$	$\log(0.14)$	No prior adopted
$\log M_c$	$\log(2.3 \times 10^{13})$	No prior adopted
$\log \beta$	$\log(4.09)$	No prior adopted
$\log M_{1,0}$	$\log(2.2 \times 10^{10})$	0.5 (in $\log M_{1,0}$ )
Astrophysics (Nuisance)		
$A_{\text{DK15}}$	1	0.3
$A_{\text{e,norm}}$	1	0.2
Halo mass		
$\log M_{\text{thre},1}$	12	0.3 (in $\log M_{\text{thre},1}$ )
$\log M_{\text{thre},2}$	13	0.3 (in $\log M_{\text{thre},2}$ )
$\log M_{\text{thre},3}$	14	0.3 (in $\log M_{\text{thre},3}$ )
FRB redshifts		
$\alpha$	3.5	No prior adopted

for a realistic forecast of parameter constraints. Thus, we compute the Fisher matrix as follows:

$$\mathbf{F} = \mathbf{F}_{\text{model}} + \mathbf{F}_{\text{prior}}, \quad (51)$$

where  $\mathbf{F}_{\text{model}}$  is computed from Eq. (50) with the power spectra of  $C_{\text{hD}}$ , and  $\mathbf{F}_{\text{prior}}$  represents the prior information. We assume that the loose prior on the  $i$ -th parameter is given by Gaussian with the variance,  $\sigma_{\text{prior},i}$ . In this case, the prior term is expressed as  $F_{\text{prior},ij} = \delta_{ij}^{\text{K}} \sigma_{\text{prior},i}^{-2}$ .

Table 2 summarises the fiducial value of the parameter to compute  $\mathbf{F}_{\text{model}}$  and the loose prior width of  $\sigma_{\text{prior},i}$ . Notably, the mass selection function (or  $M_{\text{thre}}$  in our case) and the stellar-to-halo mass relation ( $M_{1,0}$ ) can be tightly constrained from other methods, such as stacked weak lensing (e.g. Hikage et al. 2013; Zu & Mandelbaum 2015; Murata et al. 2018) and abundance matching analyses (e.g. Behroozi et al. 2013, 2019). We also include the prior information of  $A_{\text{e,norm}}$ , which is broadly consistent with the analysis in Li et al. (2020) who provided an observational constraint on  $f_{\text{e}}$  using the DM- $z$  relation from five localised FRBs.

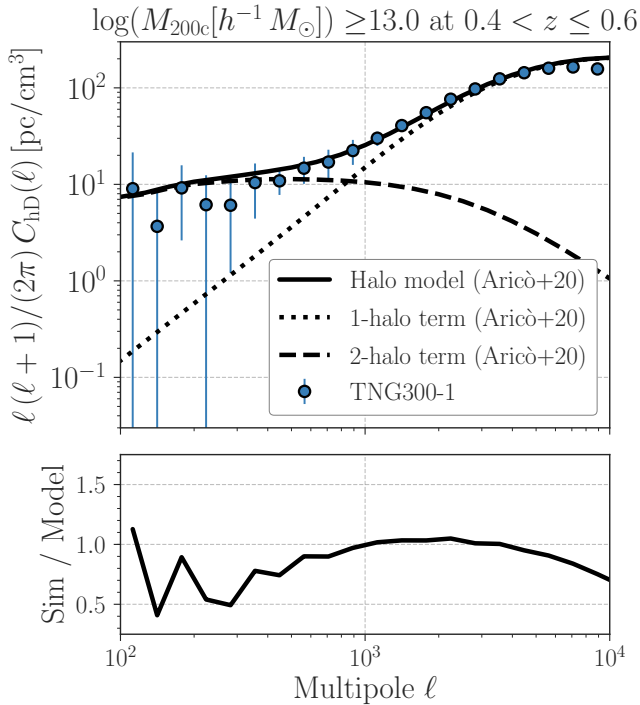


**Figure 2.** Comparison of our fiducial model of the cross power spectrum of cosmic DM and dark matter haloes (Eq. [21] with Eq. [22]) with the counterpart measured in the TNG simulation. We here consider the mass-limited halo sample with  $M \geq 10^{13} h^{-1} M_{\odot}$  at the redshift of  $0.4 < z \leq 0.6$  and assume that all the FRBs locate at  $z_s = 1$ . The selected haloes mimic a large sample of massive galaxies observed in the SDSS-III’s Baryon Oscillation Spectroscopic Survey (Nuza et al. 2013). The blue circles with error bars in the upper panel show the power spectrum in the simulation, while the solid line represents our fiducial model. The dotted and dashed lines stand for 1-halo and 2-halo terms, respectively. In the upper panel, the error bars are the standard deviations over 27 realisations of the TNG-based light-cone catalogues (Takahashi et al. 2021). The error bars simply scale as  $[(\text{survey area})/(36 \text{ deg}^2)]^{-1/2}$ , but the source number density is set to  $900^2 \text{ deg}^{-2} = 810,000 \text{ deg}^{-2}$  (the size of error bars is unrealistically small for a fixed survey area). The bottom panel shows the ratio of the simulated power spectrum with our model.

## 5 RESULTS

### 5.1 Comparisons of our model and TNG

We first compare our fiducial model of the cross power spectrum  $C_{\text{HD}}$  with the counterpart in the TNG300-1 simulation (Marinacci et al. 2018; Naiman et al. 2018; Nelson et al. 2018; Pillepich et al. 2018; Springel et al. 2018). The TNG team computed the astrophysical processes (such as gas dynamics, star formation and AGN feedback) and the gravitational evolution using the moving-mesh code AREPO (Springel 2010). The box size was  $205 h^{-1} \text{ Mpc}$  with the number of particles being  $N_p = 2500^3$ , where  $N_p$  is the same for baryon and dark matter particles at the starting redshift ( $z = 127$ ).<sup>7</sup> Each baryon

<sup>7</sup> At the initial redshift, there are  $2500^3$  gas particles in the simulation, while no stars and black holes exist. As time evolves, star formation begins in high-density regions, where some gas particles are destructed and stellar or black-hole particles are produced with certain conditions. This process does not exactly conserve the number of baryon particles, and thus  $N_p$  for baryons slightly decreases from the initial number ( $2500^3$ ).

particle has one of three forms: gas, star or black hole. Free electrons are included in the gas particles.

Mock DM maps have been computed from the projection of gas particles in the TNG simulations at different redshifts in a light cone. We use 27 realisations<sup>8</sup> of the light-cone catalogues of dark matter haloes and DM maps in Takahashi et al. (2021). Single light-cone halo catalogues and DM maps cover a sky coverage of  $6 \times 6 \text{ deg}^2$  in which  $5400^2$  light rays are homogeneously emitted from the observer; i.e. the resulting angular resolution is 4 arcsec (= 6 deg/5400). To increase the number of realisations, the simulation coordinates were randomly shifted and swapped when defining the light cone in their ray-tracing pipeline. We select dark matter haloes by imposing  $M_{200c} \geq 10^{13} h^{-1} M_{\odot}$  and  $0.4 < z \leq 0.6$  in the light-cone catalogues and then perform the cross-correlation analysis with DM maps at the source redshift of  $z_s = 1$ . Notably, the simulated DM maps do not contain the contribution from  $D_{\text{MW}}$ . We set  $\Delta\theta_{\text{FRB}} = 0$  in the cross-correlation analysis for simplicity. We summarise how to measure the power spectrum from the simulation data and results for halo samples as varying the selection of halo masses and redshifts in Appendix B.

Figure 2 shows our baseline model of the cross power spectrum and comparisons with the simulation results. The dashed line in the upper panel is the 2-halo term arising from the two-point correlation between separated haloes (Eq. [24]), whereas the solid line includes the correlation sourced by free electrons inside single haloes (Eq. [22]). At  $\ell \gtrsim 10^3$  (corresponding angular scale of  $\lesssim 3$  arcmin), the 2-halo term becomes subdominant, and most cross-correlation signals can be explained by free electrons inside haloes. We find that our model provides a reasonable fit to the simulation result for  $\ell \lesssim 10^4$ , although the model of free electrons is not calibrated with electron density profiles in the hydrodynamical simulation (see, Aricò et al. 2020, for details of the calibration).

Note that our model is phenomenological and relies on various fitting formulas for large-scale structures. To further improve the model precision, we may need to consider various points, such as possible changes of the polytropic index of gas density at central regions of haloes (see e.g. McDonald et al. 2013, for examples of cluster-sized haloes), non-linear halo bias (e.g. Mead & Verde 2021) and baryonic effects on statistical properties of haloes (e.g. Bocquet et al. 2016; Beltz-Mohrmann & Berlind 2021). These points should be considered in the near future; they are beyond the scope of this study. We revisit the limitation of our model in Subsection 6.1.

### 5.2 Information contents

#### 5.2.1 Parameter dependence

Next, we study the dependence of the cross power spectrum on model parameters. Figure 3 shows some representative examples of predicted power spectra as varying relevant cosmological and astrophysical parameters. In this figure, we consider seven cases as follows:

- (i) Fiducial cosmological and astrophysical parameters as listed in Table 2;
- (c-i) The cosmology with a higher  $\sigma_8$  by 0.07 and the fiducial astrophysics;
- (c-ii) The cosmology with a higher  $\Omega_b$  by 10% and the fiducial astrophysics;

<sup>8</sup> In the previous work (Takahashi et al. 2021), 10 DM maps were prepared. In this paper, we added 17 mock maps repeating the same procedure.

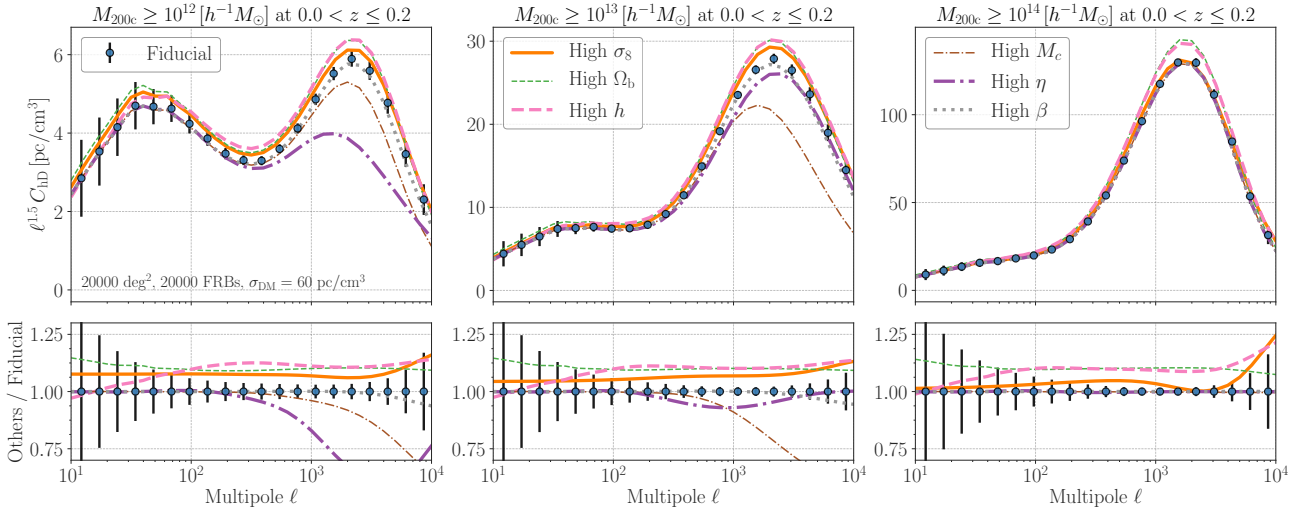


**Figure 3.** The parameter dependence of cross power spectra between haloes and DM. The left, middle and right panels show the power spectrum for the mass-limited samples with  $M \geq 10^{12}$ ,  $10^{13}$  and  $10^{14} h^{-1} M_{\odot}$  at  $0 < z \leq 0.2$ , respectively. Each top panel shows the change of the power spectra as varying the cosmological parameters of  $\Omega_b$ ,  $h$  and  $\sigma_8$ , and the astrophysical parameters of  $M_c$ ,  $\eta$  and  $\beta$  (see Table 1 and Subsection 3.2 for details about our model of gas). In the bottom, we show the fractional difference among the power spectra. The error bars in this figure is set by the Gaussian statistical uncertainty for the survey sky coverage of 20000 deg<sup>2</sup>, the mean FRB number density of 1 deg<sup>-2</sup> and the variance of host-galaxy DM being 60 pc/cm<sup>3</sup>. We here do not include the beaming effect due to localisation errors of FRBs for simplicity. The blue points represent our fiducial model with the best-fit cosmological model by Planck Collaboration et al. (2016) and the astrophysics mimicking the TNG simulation (Springel et al. 2018), while the orange solid, green dotted, pink dashed, brown dashed-dotted, purple dashed-dotted and grey dotted lines are the models with higher  $\sigma_8$ ,  $\Omega_b$ ,  $h$ ,  $M_c$ ,  $\eta$  and  $\beta$ , respectively. Note that  $M_c$  gives a halo mass scale above which more than half of gas in the halo is bound,  $\eta$  determines a typical distance scale of ejected gas from the halo centre due to feedback processes, and  $\beta$  controls the gas-to-halo mass relation.

(c-iii) The cosmology with a higher  $h$  by 10% and the fiducial astrophysics;

(a-i) The fiducial cosmology and the astrophysical model with a higher  $M_c$  by 0.2 dex (= 58.4%);

(a-ii) The fiducial cosmology and the astrophysical model with a higher  $\eta$  by 0.2 dex;

(a-iii) The fiducial cosmology and the astrophysical model with a higher  $\beta$  by 0.2 dex.

We now consider the mass-limited samples of  $M_{200c} \geq 10^{12}$ ,  $10^{13}$  and  $10^{14} h^{-1} M_{\odot}$  at the redshift of  $0 < z \leq 0.2$ . We adopt Eq. (14) for the redshift distribution of FRBs from this section. In each panel, the blue circles with error bars show the model (i), whereas the orange solid, green dotted, pink dashed, brown dashed-dotted, purple dashed-dotted and grey dotted lines represent model (c-i), (c-ii), (c-iii), (a-i), (a-ii) and (a-iii), respectively. The black error bars are estimated as in Subsection 4.3 when the sky coverage of 20000 deg<sup>2</sup>,  $\bar{n}_{\text{FRB}} = 1$  deg<sup>-2</sup> and  $\sigma_{\text{DM}} = 60$  pc/cm<sup>3</sup> are adopted. In the figure, we ignore the beaming effect  $\mathcal{B}(\ell)$  for simplicity. Note that the cross power spectrum will be exponentially suppressed at  $\ell \gtrsim 3800 (\Delta\theta_{\text{FRB}}/3 \text{ arcmin})^{-1}$  if the beaming effect is included. In each panel in the figure, the bump in  $\ell^{1.5} C_{\text{hD}}$  at  $\ell \lesssim 100$  is determined by the 2-halo term, whereas the counterpart at  $\ell \gtrsim 1000$  is dominated by the 1-halo term.

### Cosmological dependence

Models (c-i)–(c-iii) highlight the cosmological dependence on the cross power spectrum. A higher  $\Omega_b$  can increase the abundance of free electrons in the universe, enhancing the cross power spectra regardless of the halo mass threshold. A similar enhancement can be seen when one increases the Hubble parameter  $h$  because the overall amplitude of cosmic DM scales with  $\Omega_b h$  (see Eqs. [9] and [10]).

Nevertheless, the cross-correlation allows us to break the degeneracy of  $\Omega_b$  and  $h$  using the 2-halo term. The 2-halo term is proportional to the linear matter power spectrum  $P_L$ , and the location of the peak of  $P_L$  is determined by the scale of matter-radiation equality. The comoving wave number at the peak relates with the horizon scale at the matter-radiation equality and varies with  $\Omega_M h^2$  (e.g. Eisenstein & Hu 1998). Hence, increasing  $h$  can make the 2-halo term of  $C_{\text{hD}}$  shift toward higher  $\ell$ . This effect causes the difference of the 2-halo term between models (c-ii) and (c-iii). The dependence of the 1-halo term on  $\Omega_b$  and  $h$  is also helpful to break the degeneracy because the halo concentration can depend on the shape of  $P_L$ , which is determined by the physical baryon density  $\Omega_b h^2$ . Notably, the parameters of  $\Omega_b$  and  $h$  can change the shape of  $C_{\text{hD}}$  compared with the fiducial case, whereas the fraction of electrons in cosmic baryon density  $f_e$  changes the amplitude of  $C_{\text{hD}}$  alone. Hence, a detailed cross-correlation analysis enables us to break the degeneracy among  $\Omega_b$ ,  $h$  and  $f_e$ . Note that the cross-correlation with galaxies at different redshifts can provide information of the redshift dependence of  $f_e$  in principle.

Because the halo concentration  $c_h$  increases with  $\sigma_8$  (e.g. Ludlow et al. 2014), the gravitational potential of a halo deepens, and baryons can be more concentrated in our model. This effect makes the 1-halo term of  $C_{\text{hD}}$  higher as  $\sigma_8$  increases. On the other hand, the  $\sigma_8$  dependence of the 2-halo term can change with a different mass threshold. The 2-halo term is proportional to  $P_L$  and the linear halo bias  $b_h$ . The halo bias for more massive haloes decreases with  $\sigma_8$ , but the bias of galaxy-sized haloes is less sensitive to  $\sigma_8$  (e.g. Mo & White 1996; Sheth & Tormen 1999). This effect makes the 2-halo term larger at lower mass-limited samples. Hence, the degeneracy between  $\Omega_b h$  and  $\sigma_8$  can be efficiently broken with multiple mass-limited samples.

For other cosmological parameters, we briefly summarise promi-

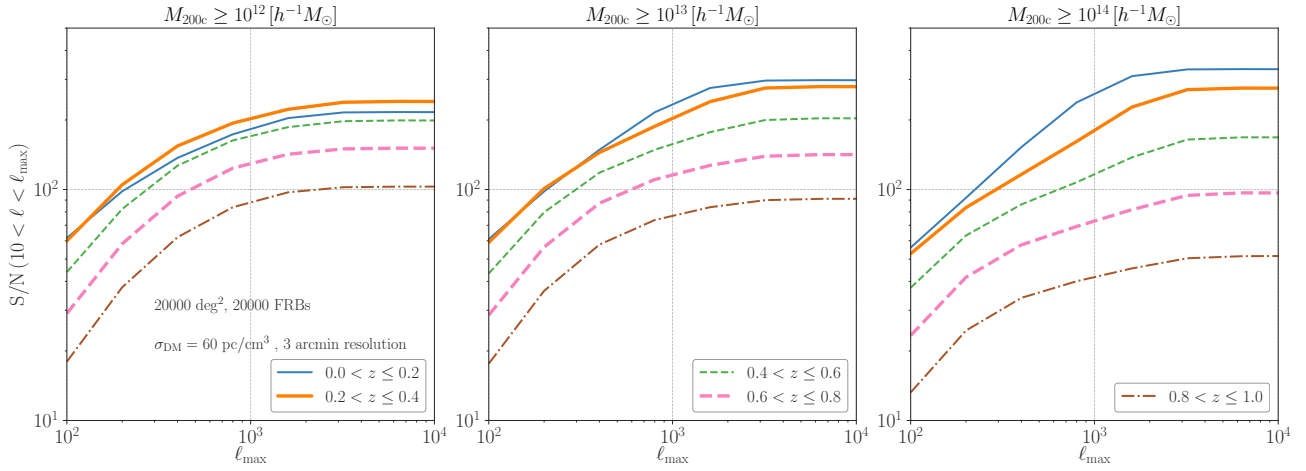


**Figure 4.** The cumulative SNR ( $S/N$ ) of cross power spectra between DM and dark matter haloes. In each panel, we show the SNR for a given mass-limited halo sample at different redshift bins as varying the maximum multipoles ( $\ell_{\max}$ ) used in the cross-correlation analysis. The blue thin, orange thick, green dashed, pink dash-dotted and brown dotted-dashed lines show the SNR at the redshift bin of  $0 < z \leq 0.2$ ,  $0.2 < z \leq 0.4$ ,  $0.4 < z \leq 0.6$ ,  $0.6 < z \leq 0.8$  and  $0.8 < z \leq 1.0$ , respectively. The left, middle and right panels represent the results for the mass-limited samples with  $M [h^{-1}M_{\odot}] \geq 10^{12}$ ,  $10^{13}$  and  $10^{14}$ , respectively. In this figure, we assume that 20000 FRBs are available over  $20000 \text{ deg}^2$  and the variance of host-galaxy DM being  $60 \text{ pc/cm}^3$  with the localisation error of 3 arcmin. Note that a measurement with  $S/N = 100$  indicates that the amplitude of the cross power spectrum can be measured with a 1% level of precision.

ment effects in the cross-correlation analysis. The parameter  $n_s$  changes the  $\ell$  dependence of the 2-halo term at  $\ell \lesssim 100$  regardless of halo selections, whereas the change in the halo concentration by  $n_s$  affects the shape of 1-halo term. The redshift dependence of  $C_{\text{hD}}$  is useful to determine the cosmological parameters of  $\Omega_M$  and  $w_0$  because these parameters govern the expansion rate at the late-time universe (Eq. [1]). In general relativity, the expansion rate also determines the redshift dependence of the linear matter power spectrum (e.g. Linder 2005). Hence, the measurement of the 2-halo terms at different redshifts allows us to constrain  $\Omega_M$  and  $w_0$ .

#### Astrophysical dependence

The difference among models (a-i), (a-ii) and (a-iii) shows the dependence of the cross power spectrum on the astrophysical parameters. First, we find that cluster-sized haloes are less sensitive to the astrophysical parameters provided the parameters around the TNG-like values are considered. Because most baryons around clusters are made of free electrons and bound within their virial regions, the 1-halo term for the sample with  $M_{200c} \geq 10^{14} h^{-1} M_{\odot}$  is mainly determined by the amount of cosmic baryons in a cluster, scaling with  $\sim (\Omega_b/\Omega_M) M_{200c}$ . As going to lower masses, stars and ejected gas affect the 1-halo term. Increasing  $M_c$  means that the amount of bound gas decreases at  $M_{200c} \lesssim 10^{13} h^{-1} M_{\odot}$ , making the 1-halo term for  $M_{200c} \lesssim 10^{13} h^{-1} M_{\odot}$  smaller. When setting  $\eta$  larger, the amount of free electrons within a halo decreases at a fixed halo mass. Because the ejected gas plays a role in the haloes with  $M_{200c} \ll M_c$  in our model, the cross-correlation with a smaller mass  $M_{200c}$  is more sensitive to the change in  $\eta$ . The parameter  $\beta$  controls how rapidly the gas is expelled from haloes as the halo masses decrease. A larger  $\beta$  increases the amount of bound gas at  $M_{200c} > M_c$ , whereas the bound gas decreases at  $M_{200c} < M_c$ . Because our fiducial model assumes  $M_c \sim 2 \times 10^{13} h^{-1} M_{\odot}$ , the cross power spectra for the mass-limited samples of  $M_{200c} \geq 10^{12}$  and  $10^{13} h^{-1} M_{\odot}$  are affected by the change in  $\beta$ . Notably, the 2-halo terms are less sensitive to the astrophysical parameters regardless of the halo selection.

#### 5.2.2 Signal-to-noise ratio

Another important measure of the information contents is the SNR ( $S/N$ ). It is defined as follows:

$$(S/N)^2 = \sum_{\alpha\beta} D_{\alpha} \text{Cov}_{\alpha\beta}^{-1} D_{\beta}, \quad (52)$$

where our data vector  $\mathbf{D}$  is given by Eq. (49), and we define the covariance matrix in Eq. (40). In Eq. (52), the sum takes over a range of  $\ell_{\min} < \ell < \ell_{\max}$ . We perform a logarithmic binning in  $\ell$  with  $\ell_{\min} = 10$  and  $\Delta \ln \ell = 0.4$ .

Figure 4 shows the SNR as a function of  $\ell_{\max}$  when we assume that 20000 FRBs are available over  $20000 \text{ deg}^2$  and set  $\sigma_{\text{DM}} = 60 \text{ pc/cm}^3$  and the localisation error of  $\Delta\theta_{\text{FRB}} = 3 \text{ arcmin}$ . We find that a mass-limited halo sample with a higher mass threshold at lower  $z$  tends to show a larger SNR. Cross-correlation analyses with a large  $\ell_{\max}$  make the SNR higher in general, but this is not the case when we include the beaming effect, as in Eq. (39). Because we work with  $\Delta\theta_{\text{FRB}} = 3 \text{ arcmin}$  in the figure, the SNR cannot increase at  $\ell_{\max} \approx \sqrt{16 \ln 2} / \Delta\theta_{\text{FRB}} \sim 3800$  or larger. Nevertheless, our halo model predicts that the SNR for most mass-limited samples can reach an order of 100 if we will be able to use 20000 FRBs over  $20000 \text{ deg}^2$ . This indicates that the amplitude of  $C_{\text{hD}}$  can be measured with a 1% level of precision in future cross-correlation analyses. The large SNR is mainly driven by the 1-halo terms (the correlation due to free electrons in single haloes).

Figure 5 summarises how the SNR depends on the parameters for a hypothetical FRB survey. In the figure, we consider the cross power spectra of the three mass-limited samples at  $0.2 < z \leq 0.4$  in  $20000 \text{ deg}^2$ , whereas we vary one of the survey parameters of the mean number density of FRBs  $\bar{n}_{\text{FRB}}$ , the variance of host-galaxy DM  $\sigma_{\text{DM}}$  and the angular resolution of FRBs  $\Delta\theta_{\text{FRB}}$ . For the cross power spectra at  $10 < \ell < 3200$ , the available number of FRBs in a given survey coverage is a primary parameter to determine the SNR. We find that the SNR can be degraded by a factor of 2–3 when changing  $\bar{n}_{\text{FRB}} = 1 \text{ deg}^{-2}$  to  $0.1 \text{ deg}^{-2}$ . The variance of host-galaxy DM  $\sigma_{\text{DM}}$  affects the SNR as well. The SNR can change by  $\sim 1.5$ – $2$  within a plausible range of  $40 \leq \sigma_{\text{DM}} [\text{pc/cm}^3] \leq 80$ . To extract

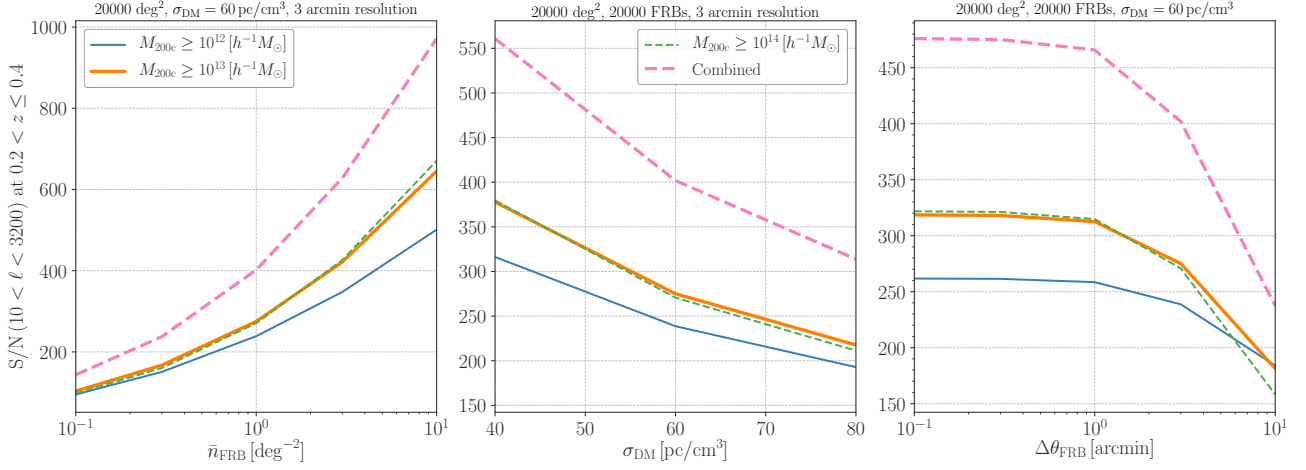


**Figure 5.** Similar to Figure 4, we vary survey parameters in a hypothetical FRB survey with a sky coverage of  $20000 \text{ deg}^2$ . In each panel, we show the SNR for the cross power spectra at  $0.2 < z \leq 0.4$  when setting a range of  $10 < \ell < 3200$ . The left panel assumes that FRB catalogues with a variance of host-galaxy DM being  $\sigma_{\text{DM}} = 60 \text{ pc/cm}^3$  and an angular resolution of FRBs being  $\Delta\theta_{\text{FRB}} = 3 \text{ arcmin}$ , while we vary the number density of FRBs  $\bar{n}_{\text{FRB}}$ . The middle panel sets the fiducial values of  $\bar{n}_{\text{FRB}} = 1 \text{ deg}^{-2}$  and  $\Delta\theta_{\text{FRB}} = 3 \text{ arcmin}$ , while we vary  $\sigma_{\text{DM}}$ . The right panel represents the  $\Delta\theta_{\text{FRB}}$  dependence of the SNR when we set  $\bar{n}_{\text{FRB}} = 1 \text{ deg}^{-2}$  and  $\sigma_{\text{DM}} = 60 \text{ pc/cm}^3$ . The blue thin, orange thick and green dashed lines are the SNRs for the mass-limited samples with  $M [h^{-1} M_{\odot}] \geq 10^{12}, 10^{13}$  and  $10^{14}$ , while the pink dashed line shows the combined SNR for the three mass-limited samples. Note that the combined analysis with different mass-limited samples is still meaningful because the cross-correlation signal is mainly determined by a majority of halos in each sample.

full information in the power spectra at  $10 < \ell < 3200$ , we require an angular resolution of 1 arcmin. The figure indicates that collecting many FRBs without a detailed localisation is not optimal to have a great SNR at  $\ell \lesssim 3000$ .

### 5.3 Fisher forecasts

We now summarise the results of our Fisher analysis on physical parameters, which are relevant to the cross power spectra between haloes and DM. We examine three hypothetical FRB data with  $(\bar{n}_{\text{FRB}}, \Delta\theta_{\text{FRB}}) = (1 \text{ deg}^{-2}, 3')$ ,  $(0.1 \text{ deg}^{-2}, 1')$ , and  $(10.0 \text{ deg}^{-2}, 10')$  to bracket possible configurations of future FRB surveys. Note that we set the variance of host-galaxy DM  $\sigma_{\text{DM}} = 60 \text{ pc/cm}^3$  for every result in this subsection.

Table 3 provides a summary of our Fisher forecasts of six cosmological parameters ( $h, w_0, \Omega_M, \Omega_b, \sigma_8$  and  $n_s$ ), three gas parameters ( $\eta, M_c$  and  $\beta$ ), one nuisance parameter for the fraction of free electrons in cosmic baryon density  $A_{e,\text{norm}}$  and one parameter for the FRB redshift distribution  $\alpha$ . In the table, we highlight that the  $1\sigma$  constraints within a 1% and 5% level of precision in red and black bold letters, respectively. Our forecasts are promising. For a given survey covering  $20000 \text{ deg}^2$ , our Fisher analysis showcases a great potential of the cross power spectra  $C_{\text{hD}}$  as follows:

- The cross power spectra can place constraints of  $w_0, \Omega_M, \sigma_8$  and  $n_s$  with a  $\sim 5\%$  level provided 20000 FRBs with an arcmin-level localisation are available. Notably, the expected constraints do not rely on any prior information from other measurements, e.g. CMB.

- The cross power spectra enable us to calibrate two astrophysical parameters of  $\eta$  and  $M_c$  with a level of 1%–2%. The former provides a typical propagation length scale of ejected gas from halo centres, whereas the latter determines a characteristic halo mass above which more than half of the gas in the halo is in a hot and bound state.

- The parameter constraint with  $(\bar{n}_{\text{FRB}}, \Delta\theta_{\text{FRB}}) = (1 \text{ deg}^{-2}, 3 \text{ arcmin})$  can be similar to the one with  $(\bar{n}_{\text{FRB}}, \Delta\theta_{\text{FRB}}) = (10 \text{ deg}^{-2}, 10 \text{ arcmin})$ . The FRB catalogues with bad localisation are still able to place meaningful constraints of

cosmology and gas physics in a wide range of halo masses, provided one can set the average number density of FRBs to  $\sim 10 \text{ deg}^{-2}$ .

- The information of  $C_{\text{hD}}$  at  $\ell \sim 10^4$  is crucial for precise estimation of physical parameters when the FRB number density is of an order of  $\sim 0.1 \text{ deg}^{-2}$ .

- The tomographic analysis with halo samples at different redshift bins is efficient to calibrate the redshift distribution of FRBs, although we require some prior knowledge to set a reasonable parametric form of the redshift distribution (see e.g. Qiang & Wei 2021).

Expected constraints of the astrophysical parameters by the cross power spectra  $C_{\text{hD}}$  can provide a powerful test for modelling cosmic baryons with hydrodynamical simulations. Figure 6 shows the expected  $1\sigma$  constraints of the three parameters of  $\eta, \beta$  and  $M_c$  in our halo model by the cross power spectra. The figure clearly demonstrates that the limits of the three parameters allow us to distinguish among possible feedback models in the evolution of baryons by cosmological hydrodynamical simulations.

### 5.4 Implications

We now summarise some implications by our Fisher analysis in Subsection 5.3. We study three subjects in modern cosmology and astrophysics: (i) global mass contents in the late-time universe at  $z < 1$ , (ii) the gas-to-halo mass relation and (iii) the impact of baryons on total matter density distributions. To do so, we generate  $10^6$  realisations of model parameters following a multivariate random Gaussian distribution with the covariance being the inverse of the Fisher matrix. Our model parameters and their central values are listed in Table 2. Using the chain of the random model parameters, we evaluate an expected confidence level of some derived parameters, which are more relevant to subjects (i)–(iii). When generating the random model parameters, we set the Fisher matrix by assuming a hypothetical FRB survey with  $\bar{n}_{\text{FRB}} = 1 \text{ deg}^{-2}$ ,  $\sigma_{\text{DM}} = 60 \text{ pc/cm}^3$  and  $\Delta\theta_{\text{FRB}} = 3 \text{ arcmin}$ . We include a non-informative prior term in the Fisher matrix (Table 2). We use the information on a set of the

**Table 3.** Summary of the Fisher forecast of the cosmological and astrophysical parameters by the cross-correlation analysis with DM and dark matter haloes. We assume an effective survey area to be  $20000 \text{ deg}^2$  used for the analysis. We consider three mass-limited samples with  $M \geq 10^{12}, 10^{13}$  and  $10^{14} h^{-1} M_\odot$  at five separated redshift bins covering up to  $z = 1$ . For a hypothetical FRB catalogue, we examine three cases of  $(\bar{n}_{\text{FRB}}, \Delta\theta_{\text{FRB}}) = (1 \text{ deg}^{-2}, 3')$ ,  $(0.1 \text{ deg}^{-2}, 1')$  and  $(10.0 \text{ deg}^{-2}, 10')$ , where  $\bar{n}_{\text{FRB}}$  is the average number density of FRBs and  $\Delta\theta_{\text{FRB}}$  is the localisation error for each FRB. In each table cell, the number without brackets show the  $1\sigma$  constraint of single parameter when we marginalise other parameters, while the number in brackets is the marginalised error divided by the fiducial parameter in percentiles. We highlight the limit within a 5% level of precision in black bold, while the red bold font represents the limit better than a 1% level of precision. The details of the Fisher analysis is provided in Subsection 4.4.

Parameters	$\ell_{\text{max}} = 3000$ w/o prior	$\ell_{\text{max}} = 3000$ w/ prior	$\ell_{\text{max}} = 10000$ w/o prior	$\ell_{\text{max}} = 10000$ w/ prior
$\bar{n}_{\text{FRB}} = 1 \text{ deg}^{-2}$ and $\Delta\theta_{\text{FRB}} = 3 \text{ arcmin}$				
$h$	0.0646 (9.61%)	0.0354 (5.26%)	0.0590 (8.76%)	0.0342 (5.08%)
$w_0$	<b>0.0422</b> (4.22%)	<b>0.0389</b> (3.89%)	<b>0.0396</b> (3.96%)	<b>0.0371</b> (3.71%)
$\Omega_{\text{M}}$	<b>0.0126</b> (4.00%)	<b>0.0109</b> (3.45%)	<b>0.0117</b> (3.71%)	<b>0.0102</b> (3.23%)
$\Omega_{\text{b}}$	0.0094 (19.05%)	0.0057 (11.64%)	0.0085 (17.26%)	0.0055 (11.22%)
$\sigma_8$	<b>0.0118</b> (1.42%)	<b>0.0088</b> (1.06%)	<b>0.0112</b> (1.35%)	<b>0.0085</b> (1.03%)
$n_s$	<b>0.0223</b> (2.31%)	<b>0.0181</b> (1.88%)	<b>0.0191</b> (1.98%)	<b>0.0160</b> (1.65%)
$\log \eta$	<b>0.0129</b> (1.51%)	<b>0.0084</b> (0.98%)	<b>0.0120</b> (1.41%)	<b>0.0079</b> (0.93%)
$\log M_c$	<b>0.0227</b> (0.17%)	<b>0.0218</b> (0.16%)	<b>0.0212</b> (0.16%)	<b>0.0204</b> (0.15%)
$\log \beta$	0.2973 (48.60%)	0.2915 (47.65%)	0.2399 (39.21%)	0.2365 (38.66%)
$A_{\text{e,norm}}$	0.2765 (27.65%)	0.1425 (14.25%)	0.2498 (24.98%)	0.1377 (13.77%)
$\alpha$	<b>0.0277</b> (0.79%)	<b>0.0270</b> (0.77%)	<b>0.0270</b> (0.77%)	<b>0.0263</b> (0.75%)
$\bar{n}_{\text{FRB}} = 0.1 \text{ deg}^{-2}$ and $\Delta\theta_{\text{FRB}} = 1 \text{ arcmin}$				
$h$	0.1457 (21.67%)	0.0483 (7.19%)	0.1117 (16.60%)	0.0451 (6.71%)
$w_0$	0.1061 (10.61%)	0.0885 (8.85%)	0.0826 (8.26%)	0.0723 (7.23%)
$\Omega_{\text{M}}$	0.0309 (9.80%)	0.0222 (7.04%)	0.0237 (7.53%)	0.0177 (5.61%)
$\Omega_{\text{b}}$	0.0191 (38.85%)	0.0077 (15.70%)	0.0141 (28.72%)	0.0072 (14.69%)
$\sigma_8$	<b>0.0282</b> (3.39%)	<b>0.0171</b> (2.06%)	<b>0.0233</b> (2.80%)	<b>0.0145</b> (1.74%)
$n_s$	0.0529 (5.49%)	<b>0.0351</b> (3.64%)	<b>0.0304</b> (3.15%)	<b>0.0212</b> (2.20%)
$\log \eta$	<b>0.0297</b> (3.47%)	<b>0.0159</b> (1.87%)	<b>0.0227</b> (2.66%)	<b>0.0113</b> (1.32%)
$\log M_c$	<b>0.0535</b> (0.40%)	<b>0.0500</b> (0.37%)	<b>0.0365</b> (0.27%)	<b>0.0353</b> (0.26%)
$\log \beta$	0.6753 (110.39%)	0.6540 (106.92%)	0.3248 (53.09%)	0.3177 (51.94%)
$A_{\text{e,norm}}$	0.5906 (59.06%)	0.1644 (16.44%)	0.4377 (43.77%)	0.1575 (15.75%)
$\alpha$	<b>0.0681</b> (1.95%)	<b>0.0630</b> (1.80%)	<b>0.0591</b> (1.69%)	<b>0.0544</b> (1.55%)
$\bar{n}_{\text{FRB}} = 10 \text{ deg}^{-2}$ and $\Delta\theta_{\text{FRB}} = 10 \text{ arcmin}$				
$h$	0.0599 (8.90%)	<b>0.0335</b> (4.98%)	0.0598 (8.89%)	<b>0.0334</b> (4.97%)
$w_0$	<b>0.0427</b> (4.27%)	<b>0.0400</b> (4.00%)	<b>0.0424</b> (4.24%)	<b>0.0398</b> (3.98%)
$\Omega_{\text{M}}$	<b>0.0130</b> (4.13%)	<b>0.0105</b> (3.33%)	<b>0.0129</b> (4.08%)	<b>0.0104</b> (3.30%)
$\Omega_{\text{b}}$	0.0081 (16.54%)	0.0051 (10.46%)	0.0082 (16.60%)	0.0051 (10.43%)
$\sigma_8$	<b>0.0125</b> (1.51%)	<b>0.0088</b> (1.06%)	<b>0.0125</b> (1.50%)	<b>0.0088</b> (1.06%)
$n_s$	<b>0.0227</b> (2.35%)	<b>0.0189</b> (1.96%)	<b>0.0227</b> (2.35%)	<b>0.0189</b> (1.96%)
$\log \eta$	<b>0.0174</b> (2.04%)	<b>0.0119</b> (1.39%)	<b>0.0173</b> (2.03%)	<b>0.0118</b> (1.39%)
$\log M_c$	<b>0.0220</b> (0.16%)	<b>0.0208</b> (0.16%)	<b>0.0220</b> (0.16%)	<b>0.0208</b> (0.16%)
$\log \beta$	0.3397 (55.53%)	0.3356 (54.87%)	0.3400 (55.59%)	0.3359 (54.91%)
$A_{\text{e,norm}}$	0.2549 (25.49%)	0.1365 (13.65%)	0.2558 (25.58%)	0.1366 (13.66%)
$\alpha$	<b>0.0241</b> (0.69%)	<b>0.0237</b> (0.68%)	<b>0.0241</b> (0.69%)	<b>0.0237</b> (0.68%)

cross power spectra with  $\ell_{\text{max}} = 3000$ . See Subsection 4.1 for the foreground haloes in our hypothetical analysis.

#### 5.4.1 Global mass contents

The CMB has been widely used to constrain the average mass density of several components so far; the CMB physics is mainly determined by density fluctuations in the early universe at  $z \sim 1100$ . Any other measurements of the density fluctuations at lower redshifts would provide a powerful test of the standard  $\Lambda$  Cold Dark Matter ( $\Lambda$ CDM) model, allowing us to explore possible deviations of the  $\Lambda$ CDM cosmology by new physics (see e.g. Weinberg et al. 2013, for a review). The fluctuations in cosmic mass density at low redshifts can be measured with weak gravitational lensing effects in galaxy images (see

e.g. Kilbinger 2015, for a review). A primary cosmological parameter in modern weak lensing surveys is given by  $S_8 = \sigma_8 (\Omega_{\text{M}}/0.3)^{0.5}$  (e.g. Jain & Seljak 1997; Hall 2021), and the latest weak lensing measurements have constrained  $S_8$  with a level of 0.02–0.03 (e.g. Hikage et al. 2019; Asgari et al. 2021; Secco et al. 2021). As the precision of the lensing measurement increases, a tension appears between the  $S_8$  inferred from the late-time lensing measurements and the counterpart predicted by the CMB constraints. The origin of this  $S_8$  tension is still under debate, while it is obviously imperative to test the tension with various approaches, which are independent of weak lensing analyses and CMB.

We expect that the cosmological signal of  $C_{\text{hD}}$  at  $\ell \lesssim 100$  and its redshift evolution offer a powerful means of determining the linear growth of density perturbations. Our Fisher analysis predicts that the cross-correlation can place a constraint of  $S_8 = 0.851 \pm 0.012$

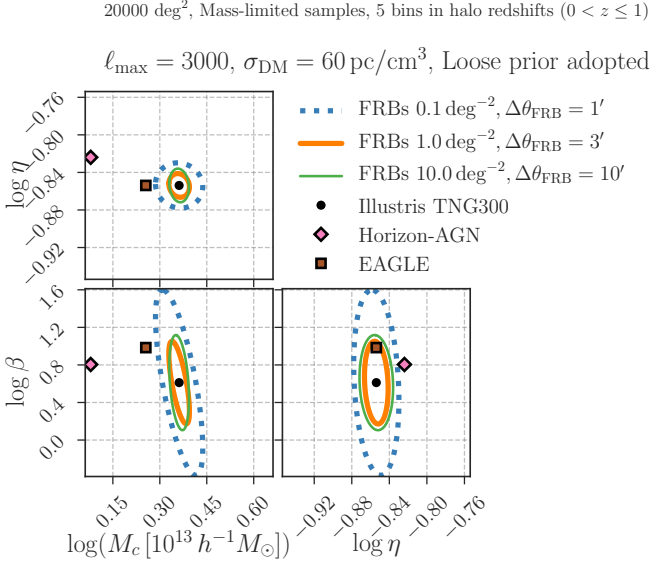


**Figure 6.** Expected  $1\sigma$  constraints of astrophysical parameters about gas in dark matter haloes. We consider three possible cases of future FRB data with  $(\bar{n}_{\text{FRB}}, \Delta\theta_{\text{FRB}}) = (1 \text{ deg}^{-2}, 3')$ ,  $(0.1 \text{ deg}^{-2}, 1')$  and  $(10 \text{ deg}^{-2}, 10')$ , where  $\bar{n}_{\text{FRB}}$  is the mean number density of FRBs and  $\Delta\theta_{\text{FRB}}$  is the localisation error. The three parameters of  $\eta$ ,  $\beta$ , and  $M_c$  provide a typical diffusion scale of gas ejected from the halo centre, the dependence of the gas mass on the halo mass, and a characteristic mass scale in the gas-to-halo mass relation (see Subsection 3.2 for details). We assume that three mass-limited samples at five redshift bins up to  $z = 1$  are available for the cross-correlation analysis. The sky coverage for the analysis is set to  $20000 \text{ deg}^2$ . We use the information about the power spectra in the range of  $10 < \ell < 3000$ . The black dot shows the best-fit gas model to the TNG simulation results (Springel et al. 2018), while the pink diamond and the brown square symbols represent the models suitable for the Horizon-AGN (Dubois et al. 2014) and EAGLE simulations (Schaye et al. 2015; Hellwing et al. 2016), respectively. See Aricò et al. (2020) for details about the calibration of the three parameters.

at a 68% confidence level. This constraint is sufficiently precise to test the  $S_8$  tension in modern cosmology. Note that the constraint of  $S_8$  is less dependent on the choice of prior in the cross-correlation analysis. Even if excluding the non-informative prior, our Fisher analysis shows that  $S_8 = 0.851^{+0.012}_{-0.013}$  (68%) can be realised with the cross-correlation analysis.

The mean baryon density has been precisely determined by the CMB and big-bang nucleosynthesis; these probes rely on the physics in the primordial photon-baryon plasma. Measurements of  $\Omega_b$  at low redshifts are always crucial because they should provide a valuable check for the understanding of the baryonic universe. Macquart et al. (2020) provided a 10%-level constraint of  $\Omega_b h$  with the relation between observed DM and host-galaxy redshifts. Note that the limit in Macquart et al. (2020) degenerates with the fraction of free electrons in cosmic baryon density,  $f_e$  in Eq. (8). Hence, other statistical observables of DM would provide some benefits to break the degeneracy among  $\Omega_b$ ,  $h$  and  $f_e$ .

As shown in Subsection 5.2.1, we found that precise measurements of the cross-correlation between DM and dark matter haloes allow breaking the degeneracy in principle. To demonstrate the constraining power of the cross-correlation, we compute confidence levels in a  $\Omega_b h - A_{e,\text{norm}}$  plane via the Fisher analysis (see Eq. [36] for the definition of  $A_{e,\text{norm}}$ ). Figure 7 shows the expected confidence levels in the  $\Omega_b h - A_{e,\text{norm}}$  plane with the cross-correlation analysis. The figure

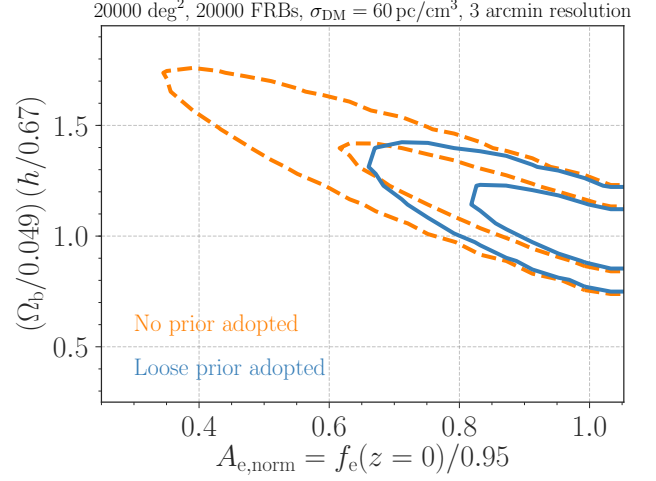


**Figure 7.** Expected constraint of  $\Omega_b h$  and  $A_{e,\text{norm}} = f_e(z=0)/0.95$ . The orange lines show 68% and 95% confidence levels derived by our Fisher analysis without any prior information, while the blue lines represent the counterparts with non-informative prior (Table 2). Note that the two parameters cannot be simultaneously constrained with the relation of observed DM and host-galaxy redshifts alone (e.g. Macquart et al. 2020). We assume that 20000 FRBs are available over  $20000 \text{ deg}^2$  and the variance of host-galaxy DM is set to  $60 \text{ pc/cm}^3$ . We also assume that the uncertainty of angular positions of individual FRBs is given by 3 arcmin.

illustrates that we can constrain the two parameters simultaneously, even without any prior on  $A_{e,\text{norm}}$ . Assuming the prior of  $A_{e,\text{norm}}$  with a level of 0.2, we also find that the cross-correlation can place a constraint of  $(\Omega_b/0.049) (h/0.67) A_{e,\text{norm}} = 0.993^{+0.030}_{-0.036}$  (68%).

We also comment on the possibility of constraining the Hubble parameter  $h$  with the cross-correlation. Our fisher analysis shows that a 5%-level constraint of  $h$  can be possible if we impose a non-informative prior (see Table 3). This expected constraint is not tight enough to test the so-called Hubble tension in modern cosmology (e.g. Riess 2020, for a review); a combined analysis of the cross-correlation with the DM-redshift relation of  $\sim 100$  localised FRBs would further improve the constraint (e.g. Wu et al. 2021).

#### 5.4.2 Gas-to-halo mass relations

The gas mass as a function of the total mass in a halo, referred to as gas-to-halo mass relation, is a paramount scaling relation in modern astronomy. Precise estimates of the gas-to-halo mass relation can improve the understanding of galaxy formation processes (e.g. van de Voort & Schaye 2012; Hummels et al. 2013; Ford et al. 2016; van de Voort et al. 2016; Davies et al. 2019; Lim et al. 2021). The gas-to-halo mass relation in clusters is of great interest for cluster cosmology (see e.g. Giodini et al. 2013, for a review). In addition, the gas-to-halo mass relation in galaxy-sized haloes plays an essential role in providing a theoretical interpretation of various observables. The observables include the thermal SZ effect (e.g. Greco et al. 2015; Vikram et al. 2017; Hill et al. 2018; Meinke et al. 2021), kinematic SZ effect (e.g. Hand et al. 2012; Hernández-Monteagudo et al. 2015; Schaan et al. 2016; Sugiyama et al. 2018), X-ray luminosity (e.g. Leauthaud et al. 2010; Anderson et al. 2015; Babyk et al. 2018) and some combinations (e.g. Wu et al. 2020; Schaan et al. 2021).

In our theoretical model, the gas mass for a halo of  $M$  is as follows:

$$M_{\text{gas}}(< r_{\text{out}}; M) = \int_0^{r_{\text{out}}} dr 4\pi r^2 (\rho_{\text{BG}}(r, M) + \rho_{\text{EG}}(r, M)), \quad (53)$$

where  $r_{\text{out}}$  is a boundary radius,  $\rho_{\text{BG}}$  and  $\rho_{\text{EG}}$  represent the bound and ejected components, respectively (see Subsection 3.2 for details). The astrophysical parameters in Table 1 determine the gas mass  $M_{\text{gas}}$ . Hence, we can infer the gas-to-halo mass relation within our halo-model framework from the precise measurements of the parameters of  $\eta$ ,  $M_c$ ,  $\beta$  and  $M_{1,0}$ .

Figure 8 summarises an expected constraint of the mass fraction of gas in haloes at three halo masses. In the figure, we define the gas mass fraction as  $f_{\text{gas}} = M_{\text{gas}}(< r_{200c})/M_{200c}$  at  $z = 0$ . We find that the measurement of  $C_{\text{hD}}$  in our fiducial setup can place a constraint of  $f_{\text{gas}} = (2.20^{+0.48}_{-0.30}) \times 10^{-3}$ ,  $(1.22^{+1.52}_{-0.43}) \times 10^{-2}$  and  $0.154^{+0.014}_{-0.020}$  for the haloes with their mass of  $M = 10^{12} h^{-1} M_{\odot}$ ,  $10^{13} h^{-1} M_{\odot}$  and  $10^{14} h^{-1} M_{\odot}$ , respectively. The above error is set by a 68% confidence level by our Fisher analysis. At the mass scale of  $10^{13} h^{-1} M_{\odot}$ , the error bar in  $f_{\text{gas}}$  becomes larger than two other mass scales because the mass dependence of hot gas fraction ( $\beta$  in Table 1) cannot be constrained well with our fiducial setup. To tighten the error of  $\beta$ , we would need more bins in halo-mass selections around  $M \sim 10^{13} h^{-1} M_{\odot}$ .

Lines in Figure 8 show the gas-to-halo mass relations predicted by different hydrodynamical simulations. The tight constraint of  $f_{\text{gas}}$  by the measurement of  $C_{\text{hD}}$  enables us to pin down which existing galaxy formation models can explain our baryonic universe. In addition, the cross-correlation analysis allows us to calibrate the gas-to-halo mass relation at cluster scales with a level of  $\sim 10\%$ , providing informative prior for cluster cosmology. Recalling that the small-scale cross-correlation can be sensitive to gas physics, whereas the large-scale counterpart is mostly determined by cosmology (see Subsection 5.2.1 for details). Notably, the measurement of  $C_{\text{hD}}$  scales with the number density of free electrons, whereas the X-ray luminosity varies with the density squared and can be subject to the gas clumpiness (e.g. Nagai & Lau 2011; Vazza et al. 2013; Battaglia et al. 2015).

#### 5.4.3 Sub-grid physics in hydrodynamical simulations

Although most cosmic mass densities comprise dark matter, baryons still affect the statistical properties of total mass density distributions in the universe (see Chisari et al. 2019, for a review). Hydrodynamical simulations are the most accurate techniques for predicting the impact of baryons on fluctuations in the cosmic mass density; the simulation itself has a fundamental limitation of the resolution of masses or length scales. To include astrophysical processes associated with scales shorter than the resolution limit, the hydrodynamical simulation requires the implementation of various sub-grid recipes. Some relevant processes include the initial mass function, supernovae and AGN feedback and metal enrichment. The sub-grid physics has to be calibrated so that the simulation can explain observations, and its impact can be dependent on the assumed cosmology in the simulation. Because a cosmological hydrodynamical simulation is very time-consuming in general, a flexible method to evaluate the baryonic effects on the matter-density fluctuations is demanded.

Recently, van Daalen et al. (2020) analysed various hydrodynamical simulations to study how the sub-grid physics recipes affect the matter power spectrum. Regardless of details in the recipes, they found a tight correlation (with a  $\sim 1\%$ -level scatter) between the mean baryon fraction inside haloes and the power spectrum suppression. For a comoving wave number of  $k$  in units of  $h \text{ Mpc}^{-1}$ , the

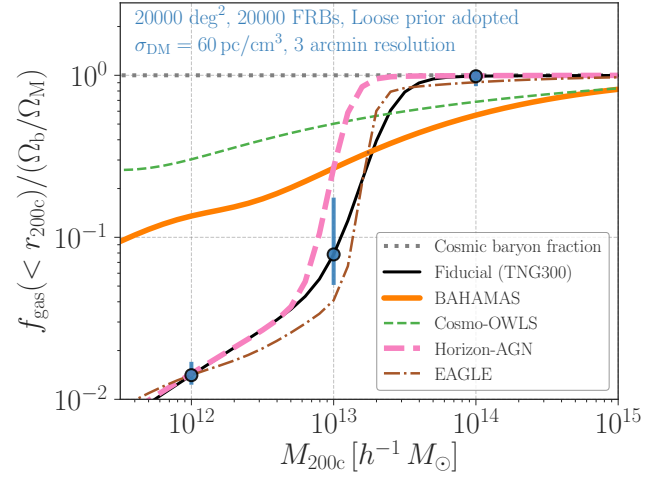


**Figure 8.** Expected constraints of the gas mass fraction at three halo masses of  $M_{200c} = 10^{12}$ ,  $10^{13}$  and  $10^{14} h^{-1} M_{\odot}$  at  $z = 0$ . We compute the gas mass fraction within the radius of  $r_{200c}$ , divided by the cosmic baryon fraction ( $\Omega_b/\Omega_M$ ). The blue points with error bars show the limits with a 68% confidence level, derived via our Fisher analysis of the cross power spectra between dark matter haloes and DM. We assume that 20000 FRBs are available in the sky of  $20000 \text{ deg}^2$  and set the variance of host-galaxy DM and the localisation error to  $60 \text{ pc/cm}^3$  and  $3 \text{ arcmin}$ , respectively. The solid black line shows our fiducial gas-to-halo mass relation expected in the TNG simulation. The other lines represent the relations for the other hydrodynamical simulations.

correlation at  $z = 0$  is approximated as follows:

$$\frac{P_{\text{w/baryon}}}{P_{\text{No baryon}}} - 1 = - \frac{2^a + 2^b (c \tilde{f}_{\text{bar},200c})^{b-a}}{k^{-a} + (c \tilde{f}_{\text{bar},200c})^{b-a} k^{-b}} \exp(d \tilde{f}_{\text{bar},200c} + e), \quad (54)$$

where  $P_{\text{w/baryon}}$  is the non-linear matter power spectrum with baryonic effects,  $P_{\text{No baryon}}$  is the matter power spectrum expected in dark-matter-only N-body simulations,  $\tilde{f}_{\text{bar},200c}$  is the baryon mass fraction in haloes of  $M_{200c} = 10^{14} M_{\odot}$  divided by  $\Omega_b/\Omega_M$ , and fitting parameters are given by  $a = 2.111$ ,  $b = 0.0038$ ,  $c = 1.371$ ,  $d = -5.816$ , and  $e = -0.4005$ . Note that Eq. (54) holds for the EAGLE, BAHAMAS, Cosmo-OWLS, IllustrisTNG and Horizon-AGN simulations. Aricò et al. (2020) also found that the  $\tilde{f}_{\text{bar},200c}$ -dependence in Eq. (54) could be explained by the gas model in Subsection 3.2 and the stellar-to-halo mass relation in Appendix A. Specifically, the baryon fraction in the model is computed as follows:

$$\tilde{f}_{\text{bar},200c} = \left[ \frac{M_{\text{gas}}(< r_{200c})}{M} + f_{\text{star}}(M) \right] \left( \frac{\Omega_b}{\Omega_M} \right)^{-1}, \quad (55)$$

where  $M_{200c} = 10^{14} M_{\odot}$ ,  $M_{\text{gas}}(< r_{200c})$  is given by Eq. (53), and  $f_{\text{star}}(M)$  is the stellar mass fraction provided in Appendix A.

Using the Fisher matrix of our astrophysical parameters ( $\eta$ ,  $M_c$ ,  $\beta$  and  $M_{1,0}$ ), we found that the expected constraint of  $\tilde{f}_{\text{bar},200c}$  by the measurements of  $C_{\text{hD}}$  is  $\tilde{f}_{\text{bar},200c} > 0.914$  (0.789) with a 68% (95%) confidence level. According to Eq. (54), this lower limit of  $\tilde{f}_{\text{bar},200c}$  can provide a stringent limit of  $|P_{\text{w/baryon}}/P_{\text{No baryon}} - 1| \lesssim 0.03$  at  $k = 1 h \text{ Mpc}^{-1}$  at the 95% confidence level. Hence, the cross power spectrum with dark matter haloes and FRBs has a great potential of constraining the baryonic effect on the small-scale matter power

spectrum, which is the main theoretical uncertainty in weak lensing cosmology today (see e.g. Mandelbaum 2018, for a review).

## 6 LIMITATIONS

Before concluding, we summarise the major limitations in our correlation statistics between dark matter haloes and cosmic DMs. The following issues will be addressed in future studies.

### 6.1 Precise calibration of halo model

As shown in Subsection 5.1 and Appendix B, our model of gas in a halo can provide a fit to the power spectra in the TNG simulation within a level of  $\sim 25\%$  over a wide range of angular scales, halo masses and redshifts. Nevertheless, the 25%-level precision in our model is insufficient to obtain unbiased estimates of the cosmological and astrophysical parameters from future measurements of  $C_{\text{hD}}$ . We now list points to be considered for more precise models of  $C_{\text{hD}}$  below.

Provided that the localisation error of FRBs is set to  $O(1)$  arcmin, the smallest relevant comoving scale to  $C_{\text{hD}}$  is of an order of  $\sim 200$  kpc at  $z = 0.1$  and becomes larger as  $z$  increases. For galaxy-sized haloes, the scale of 200 kpc provides a typical expansion of the circumgalactic medium (see e.g. Tumlinson et al. 2017, for a review). On the other hands, 200 kpc corresponds to a central region of cluster-sized haloes. Gas cooling due to some strong feedback at the cluster core must be accounted for, while various observational information about the ‘warm’ circumgalactic medium at the edge of galaxy-sized haloes would be useful (e.g. Singh et al. 2018; Mas-Ribas & Hennawi 2018).

When applying actual data of galaxies and clusters, we also require more realistic recipes to include satellite galaxies and the scatter in mass-to-observable relations for galaxy clusters. A halo occupation model (e.g. Berlind et al. 2003) and/or forward modelling approach (e.g. Lima & Hu 2005) would be promising. Further, the scatter in the gas-to-halo mass relation can be linked to some secondary halo parameters, such as shapes, ages and mass accretion rates (e.g. Green et al. 2020, for a cluster scaling relation). Our model cannot account for possible correlations between the selection function of haloes and secondary halo parameters.

On larger scales beyond the virial regions of haloes, the clustering of two separated haloes mainly contributes to the expected signal of  $C_{\text{hD}}$ . We adopt a linear bias to compute the clustering signal as in Eq. (26), but it is an inaccurate approximation at scales of  $O(10 \text{ Mpc})$  (e.g. Mead & Verde 2021). At sufficient large scales, our model predicts that the signal of  $C_{\text{hD}}$  scales with  $\sim b_{\text{h}} f_{\text{e}}$ , where  $b_{\text{h}}$  is the linear halo bias and  $f_{\text{e}}$  is the fraction of free electrons in the cosmic baryon number density. The SNR of the clustering signal can reach  $\sim 10\text{--}50$  if 20000 FRBs in a sky coverage of  $20000 \text{ deg}^2$  are available (see Figure 4). This indicates that we would require a model of  $f_{\text{e}}$  with a 2%-level precision, but our model of  $f_{\text{e}}$  still relies on phenomenological fitting functions based on the TNG simulation (Takahashi et al. 2021). A more physically motivated description of  $f_{\text{e}}$  is demanded to consider some galactic feedback processes. Notably, our model can not fully account for warm-hot intergalactic medium (WHIM) in cosmic filaments (Cen & Ostriker 1999). The ejected gas components in our model may be responsible for some parts of WHIM; we completely ignore the accretion of flesh gas through the filaments.

### 6.2 Realistic statistical errors

We employ a Gaussian approximation to compute the statistical errors of the cross power spectrum  $C_{\text{hD}}$ . Non-linear gravitational growth in cosmic mass density can induce a complex coupling of density fluctuations with different Fourier modes. The mode coupling effect causes a four-point correlation among relevant observables and increases the statistical errors (e.g. Takada & Hu 2013). For example, Connor & Ravi (2021) claimed the detection of a large average DM from nearby dark matter halos of galaxies at distances of  $< 40 \text{ Mpc}$ . Such nearby objects can induce additional scatters of our cross-correlation and affect the parameter inference in principle. The additional sample variance can be interpreted as the four-point correlation arising from Poisson number fluctuations of galaxies in the survey window (see e.g. Sato et al. 2009; Osato & Takada 2021, for other cosmological observables). Although the four-point correlation can be computed in a halo-model approach, we leave its impact on parameter forecasts for future studies.

In practice, the localisation error of FRBs may depend on the sky coordinate of FRBs, making the beaming function of Eq. (39) more complicated (e.g. Rafiei-Ravandi et al. 2021). More realistic treatments of the localisation error would be needed in actual measurements of  $C_{\text{hD}}$ . The redshift distribution of FRBs is a key ingredient in the cross-correlation analysis. A set of localised FRBs with sub-arcseconds is needed to have a reasonable estimate of the redshift distribution. Target selection in a small sky coverage may be subject to the sample variance (see e.g. Cunha et al. 2012, for similar studies in the light of photometric redshifts in galaxy imaging surveys). It would be interesting to study how many FRBs have to be localised with a level of sub-arcseconds and how wide sky coverage is required for a precise inference of the redshift distribution. The one-point probability distribution of observed DMs can provide complementary information about the redshift distribution of FRBs (Shirasaki et al. 2017). In addition, we may use another FRB observable of the scattering time<sup>9</sup> to control the variance of the host-galaxy DM (e.g. Chawla et al. 2021; Cordes et al. 2021), but more investigations would be required.

### 6.3 DMs from FRB sources

We have ignored possible contributions from interstellar media or stellar discs at FRB sources (i.e., basically from the host galaxies) to the cross-correlation analysis, although this contribution is largely dependent on the origin of FRBs. We now provide a rough order-of-magnitude estimate based on a halo model.

We first assume that the physical sizes of FRB sources are small enough to be approximated as point sources. This assumption is expected to be valid provided FRBs are associated with astrophysical compact objects (e.g. Bhandari et al. 2020a), and we work with scales larger than  $\sim 100 \text{ kpc}$ . Then, we write cumulative DMs from FRB sources as follows:

$$D_{\text{source}}(\theta) = \frac{1}{\mathcal{N}_{\text{FRB}}} \int_0^{\chi_H} d\chi \chi^2 f_{\text{duty}}(\chi) \int dM \frac{dn}{dM}(M, \chi) \times P(M, z(\chi)) \bar{\tau}_s [1 + \delta_{\text{h}}(\chi\theta, \chi; M)], \quad (56)$$

$$\mathcal{N}_{\text{FRB}} = \int_0^{\chi_H} d\chi \chi^2 f_{\text{duty}}(\chi) \int dM \frac{dn}{dM}(M, \chi) P(M, z(\chi))$$

<sup>9</sup> A FRB pulse can be broadened because of multi-path propagation by scattering (e.g. Blandford & Narayan 1985). The scattering time provides a typical time scale of the temporal broadening of FRBs by the scattering due to electron density variations along a line of sight.

where  $P(M, z)$  represents the number of FRB sources in a halo of mass  $M$  at the redshift  $z$ ,  $\bar{\tau}_s$  is the column density of free electrons around single FRBs and  $f_{\text{duty}}(\chi)$  provides the fraction of *observed* FRBs to their total number. For simplicity, we ignore any dependence of  $\bar{\tau}_s$  on halo masses, redshifts and other properties. Notably,  $\bar{\tau}_s$  should be evaluated by the average column density over the orientation of stellar discs in FRB host haloes.

In Eq. (56), we can normalise  $P(M, z)$  by  $\int dM P(M, z) = 1$  at each redshift, without loss of generality. Using recent observational constraints in Heintz et al. (2020), we find that  $P(M, z)$  can be approximated as a log-normal distribution in terms of stellar masses<sup>10</sup>:

$$P(M, z) = P(M_{\text{star}}(M, z)) \frac{dM_{\text{star}}}{dM}, \quad (58)$$

$$P(M_{\text{star}}) = \frac{1}{M_{\text{star}} \ln 10} \frac{1}{\sigma \sqrt{2\pi}} \exp \left[ - \left( \frac{\log M_{\text{star}} - \mu}{2\sigma} \right)^2 \right], \quad (59)$$

where  $M_{\text{star}}(M, z)$  is the stellar mass (in units of  $M_{\odot}$ ) in a halo  $M$  at  $z$ ,  $\mu = 9.30$  and  $\sigma = 0.77$ . The stellar-to-halo mass relation is given in Appendix A. Then, the fraction of  $f_{\text{duty}}$  is determined so that the redshift distribution of FRBs follows Eq. (14). Specifically, we set  $f_{\text{duty}}$  by

$$p(\chi) = \chi^2 f_{\text{duty}}(\chi) \int dM \frac{dn}{dM} P(M, z(\chi)), \quad (60)$$

where the normalisation is given by  $\int d\chi p(\chi) = 1$ .

The halo model predicts that the cross-correlation between  $D_{\text{source}}$  and  $\delta_{\text{h}}^{2\text{D}}$  scales with  $\bar{\tau}_s$  and

$$f_{\text{eff,FRB}} = \frac{1}{N_{\text{FRB}}} \int_{\chi_{\text{l,min}}}^{\chi_{\text{l,max}}} d\chi \chi^2 f_{\text{duty}}(\chi) \times \int dM \frac{dn}{dM}(M, \chi) S(M) P(M, z(\chi)), \quad (61)$$

where  $f_{\text{eff,FRB}}$  represents the fraction of FRB host haloes that share the selection of halo masses and redshifts with  $\delta_{\text{h}}^{2\text{D}}$ . For mass-limited samples with  $M \geq 10^{12} h^{-1} M_{\odot}$ , our fiducial model with Eq. (58) predicts that  $f_{\text{eff,FRB}}/10^{-4} = 0.37, 1.36, 1.81, 1.69$  and  $1.32$  at  $0 < z \leq 0.2, 0.2 < z \leq 0.4, 0.4 < z \leq 0.6, 0.6 < z \leq 0.8$  and  $0.8 < z \leq 1.0$ , respectively. On the other hand, we find that  $f_{\text{eff,FRB}}$  is smaller than  $10^{-7}$  for mass-limited samples with  $M \geq 10^{14} h^{-1} M_{\odot}$  for all relevant redshift bins.

For comparison, the DM by free electrons distributed in a halo<sup>11</sup> of  $M$  in a narrow redshift range can roughly scale with

$$420 \text{ pc/cm}^3 \left( \frac{f_{\text{gas}}(M, z)}{0.15} \right) \left( \frac{M}{10^{14} M_{\odot}} \right)^{1/3} \left( \frac{H(z)}{100 \text{ km/s/Mpc}} \right)^{4/3}, \quad (62)$$

where  $f_{\text{gas}}$  is the mass fraction of gas in a halo, and it depends on the halo mass and redshift.

Suppose that a typical value of  $\bar{\tau}_s$  ranges from 100–1000 pc/cm<sup>3</sup>, we expect  $f_{\text{eff,FRB}} \bar{\tau}_s \ll 1 \text{ pc/cm}^3$  for cluster-sized haloes, while  $f_{\text{eff,FRB}} \bar{\tau}_s \sim 0.01 - 0.1 \text{ pc/cm}^3$  can be possible for galaxy-sized haloes. Hence, the cross-correlation for cluster-sized haloes is less affected by the near-source plasma, allowing us to perform a robust cosmological analysis. To constrain astrophysical parameters,

<sup>10</sup> Note that  $P(M, z)$  is poorly understood yet. A recent observation implies that a typical host halo mass of FRBs may be cluster-sized (Rafiei-Ravandi et al. 2021), but more observations are required to make a robust conclusion.

<sup>11</sup> We evaluate this as  $(X_{\text{p}} + Y_{\text{p}}/2) [f_{\text{gas}} M (2r_{200c})] [(4/3) \pi r_{200c}^3 m_{\text{p}}]^{-1}$ .

we require a cross-correlation function with less massive haloes. Because Eq. (62) gives  $\sim 0.9 \text{ pc/cm}^3$  at the mass of  $\sim 10^{12} M_{\odot}$  in our fiducial scenario ( $f_{\text{gas}}/0.15 \approx 10^{-2}$  at  $M \sim 10^{12} M_{\odot}$ ), the near-source plasma with  $f_{\text{eff,FRB}} \bar{\tau}_s \sim 0.01 - 0.1 \text{ pc/cm}^3$  may affect the cross-correlation for galaxy-sized haloes. Thus, we expect that the near-source plasma can be a major systematic source to constrain gas physics. Future studies need to develop a more realistic model of  $D_{\text{source}}$  by incorporating the physics of compact objects.

## 7 CONCLUSIONS AND DISCUSSIONS

In this article, we studied information contents in cross-correlation analyses with dark matter haloes and DMs arising from large-scale structures. Near-future observations of FRBs will allow us to perform a statistical analysis of the DM over many lines of sight. The cross-correlation of the DM and the position of dark matter haloes provides a powerful means of studying the redshift evolution in free electrons and the non-linear baryonic process of gas in single dark matter haloes. We adopted a halo-model approach to predict an expected cross-correlation signal of the DM and several mass-limited halo samples. Our halo model assumes a two-phase gas scenario, which had been calibrated with a set of hydrodynamical simulations (Aricò et al. 2020). We also considered a realistic redshift evolution of the average number density in free electrons, which is consistent with the IllustrisTNG simulations (Springel et al. 2018; Takahashi et al. 2021). Our model has six parameters to set the cosmological evolution of dark matter haloes, and four parameters to characterise the gas density profile in single haloes, the gas-to-halo mass relation and the stellar-to-halo mass relation.

According to a rich phenomenology in the halo model, we improved our previous results (Shirasaki et al. 2017) by accounting for non-linear gravitational and baryonic effects in the cross-correlation analysis. Our findings in this study are summarised below.

(i) Our halo model predicts that a cross power spectrum with cluster-sized haloes at  $\ell \lesssim 10^4$  is sensitive to the cosmological parameters, but it is less affected by gas physics. Moreover, a cross power spectrum with group- and galaxy-sized haloes would contain the information about baryonic physics at angular scales of  $\lesssim 10$  arcmin. Therefore, a combined analysis of the cross-correlation with haloes at different halo masses would be efficient to constrain cosmology and astrophysics separately.

(ii) The normalisation of the cross power spectrum scales with a combination of  $\Omega_{\text{b}} h f_{\text{e}}$  ( $\Omega_{\text{b}}$ ,  $h$  and  $f_{\text{e}}$  are the mean baryon density, the present-day Hubble parameter and the fraction of free electrons in cosmic baryon density today, respectively), whereas the shape of the power spectrum is affected by  $\Omega_{\text{b}}$  and  $h$  but not by  $f_{\text{e}}$ . Hence, a detailed analysis of the cross-correlation can break the primary degeneracy of  $\Omega_{\text{b}} h f_{\text{e}}$  in principle.

(iii) Assuming that 20000 FRBs are available in a sky coverage of 20000 deg<sup>2</sup> with a plausible scatter of the DM in FRB host galaxies and the localisation error of FRBs being 3 arcmin, we found that the SNR of the cross power spectrum at  $\ell \lesssim 3000$  can reach  $\sim 100$  for haloes in a wide range of masses and redshifts. This indicates that the future FRB data will allow us to measure the cross-correlation signal with a level of  $\sim 1/100 \sim 1\%$  precision.

(iv) We performed a Fisher analysis to forecast parameter constraints with cross-correlation analyses with dark matter haloes and

the DM from the future FRB data. We found that the cosmological parameters could be constrained with a level of 5%, even if informative priors from the CMB are excluded. On the astrophysical parameters, the cross-correlation analysis could put a tight constraint of a typical propagation length scale of ejected gas from halo centres and a characteristic halo mass below which more than half of the gas in the halo comprises the ejected component.

(v) The expected parameter constraints by the cross-correlation can shed light on the tension of gravitational growth of cosmic matter density in modern cosmology because the cross-correlation with different redshift bins is efficient to trace the redshift evolution of matter density fluctuations. We expect that the cross-correlation has a potential of constraining  $S_8 = \sigma_8(\Omega_M/0.3)^{0.5}$  with a level of  $S_8 = 0.851 \pm 0.012$  (68% CL), where  $\Omega_M$  and  $\sigma_8$  represent the mean cosmic mass density and the linear mass variance smoothed by  $8 h^{-1}$  Mpc, respectively. In addition, the amplitude of the cross-correlation function can place a meaningful limit of the mean baryon density at low redshifts. The expected limit by the future cross-correlation is  $(\Omega_b/0.049)(h/0.67)(f_c/0.95) = 0.993^{+0.030}_{-0.036}$  at a 68% confidence level. These limits would provide an important consistency test of structure formation in an expanding universe based on low-redshift information alone.

(vi) The cross-correlation with haloes and DM in future FRB surveys can also place a stringent limit on the gas-to-halo mass relation and the baryon content (i.e. the sum of stars and gas) in cluster-sized haloes. The expected limit on the gas-to-halo mass relation allows us to pin down which existing galaxy formation models can explain our baryonic universe. The stringent limit of the baryon content in clusters would provide a reasonable estimate on the strength of feedback by AGN, bracketing baryonic effects on spatial clustering in large-scale structures.

Our results provide a major step forward to precision cosmology with FRBs, but there are some limitations to apply our method to future datasets. We require a more precise model for the cross-correlation between haloes and DM. Our halo model can reproduce the cross power spectra for mass-limited haloes in the TNG simulations with a level of 25%. Note that the gas model in this study has been calibrated so that it can provide a reasonable fit to non-linear matter power spectra in simulations. We expect that a direct calibration of gas density profiles around single haloes in the simulations can improve the model accuracy but leave it for future studies. In addition, more observational studies are crucial in determining the redshift distribution of FRBs at a given observational condition. We adopt a simple parametric model of the redshift distribution, but this has to be improved before a large sample of FRBs would be available. Further, we ignore possible contributions from near-source plasma in the interstellar medium (i.e., basically from the host galaxy) to the cross-correlation analysis. We provided a rough order-of-magnitude estimate of the near-source plasma in Subsection 6.3, but more realistic modelling associated with astrophysics of compact objects will be needed for future studies.

## ACKNOWLEDGEMENTS

This work is supported by MEXT KAKENHI Grant Number (19K14767, 20H04723, 20H05855, 20H05861) and Grant-in-Aid for JSPS Fellows Grant Number JP21J00011. This work is also supported by MEXT KAKENHI No. 20H01901, 20H01904, 20H00158,

18H01213, 18H01215, 17H06357, 17H06362, and 17H06131 (KI). We also thank the participants of the workshops with the identification number YITP-T-20-04 for discussions. KO is supported by JSPS Research Fellowships for Young Scientists. Numerical computations were in part carried out on Cray XC50 at Center for Computational Astrophysics, National Astronomical Observatory of Japan.

## DATA AVAILABILITY

The data underlying this article will be shared on reasonable request to the corresponding author.

## APPENDIX A: A MODEL OF STELLAR-TO-HALO MASS RELATION

In this appendix, we summarise a model of stellar masses as a function of halo masses and redshifts. We adopt the model in [Aricò et al. \(2020\)](#), which follows the parametrisation from the abundance matching analysis in [Behroozi et al. \(2013\)](#).

The stellar mass fraction in a halo is given by

$$f_{\text{star}}(M, z) = \epsilon \left( \frac{M_1}{M} \right) 10^{g(\log M_1/M) - g(0)}, \quad (\text{A1})$$

where

$$g(x) = -\log(10^{\alpha x}) + \delta \frac{[\log(1 + e^x)]^\gamma}{1 + \exp(10^{-x})}, \quad (\text{A2})$$

and  $\alpha, \delta, \gamma, \epsilon$  and  $M_1$  are redshift-dependent parameters in the model. We set the model parameters at  $z = 0$  with the results in [Kravtsov et al. \(2018\)](#), while the redshift dependence is assumed to be the same as in [Behroozi et al. \(2013\)](#). To be specific, the parameters are given by

$$\nu(a) = \exp(-4a^2), \quad (\text{A3})$$

$$\log M_1 = \log(M_{1,0}) + m_{1,a}(a-1) + m_{1,z}z, \quad (\text{A4})$$

$$\log \epsilon = \log(\epsilon_0) + \epsilon_a(a-1)\nu + \epsilon_{a,2}(a-1), \quad (\text{A5})$$

$$\alpha = \alpha_0 + \alpha_a(a-1)\nu, \quad (\text{A6})$$

$$\delta = \delta_0 + [\delta_a(a-1) + \delta_z z]\nu, \quad (\text{A7})$$

$$\gamma = \gamma_0 + [\gamma_a(a-1) + \gamma_z z]\nu, \quad (\text{A8})$$

where  $a = 1/(1+z)$  and  $m_{1,a} = -1.793, m_{1,z} = -0.251, \epsilon_0 = 0.023, \epsilon_a = -0.006, \epsilon_{a,2} = -0.119, \alpha_0 = -1.779, \alpha_a = 0.731, \delta_0 = 4.394, \delta_a = 2.608, \delta_z = -0.043, \gamma_0 = 0.547, \gamma_a = 1.319, \text{ and } \gamma_z = 0.279$ .

In this paper, we regard  $M_{1,0}$  as a single free parameter in the model and fix the other parameters.

## APPENDIX B: DETAILED COMPARISONS OF CROSS POWER SPECTRA WITH HALO MODEL AND TNG

We now compare our model of the cross power spectrum between dark matter haloes and DMs with the counterpart in the TNG simulations.

When computing the cross power spectrum, we use 27 realisations of the DM maps at source redshifts being 1 in [Takahashi et al. \(2021\)](#). We also consider three mass-limited samples of haloes for our cross-correlation analysis. We work with the halo samples with their masses greater than  $10^{12}, 10^{13}$  and  $10^{14} h^{-1} M_\odot$ . We divide the halo redshifts into five bins of  $0 < z \leq 0.2, 0.2 < z \leq 0.4, 0.4 < z \leq 0.6, 0.6 < z \leq 0.8$  and  $0.8 < z \leq 1.0$  to study the redshift dependence.

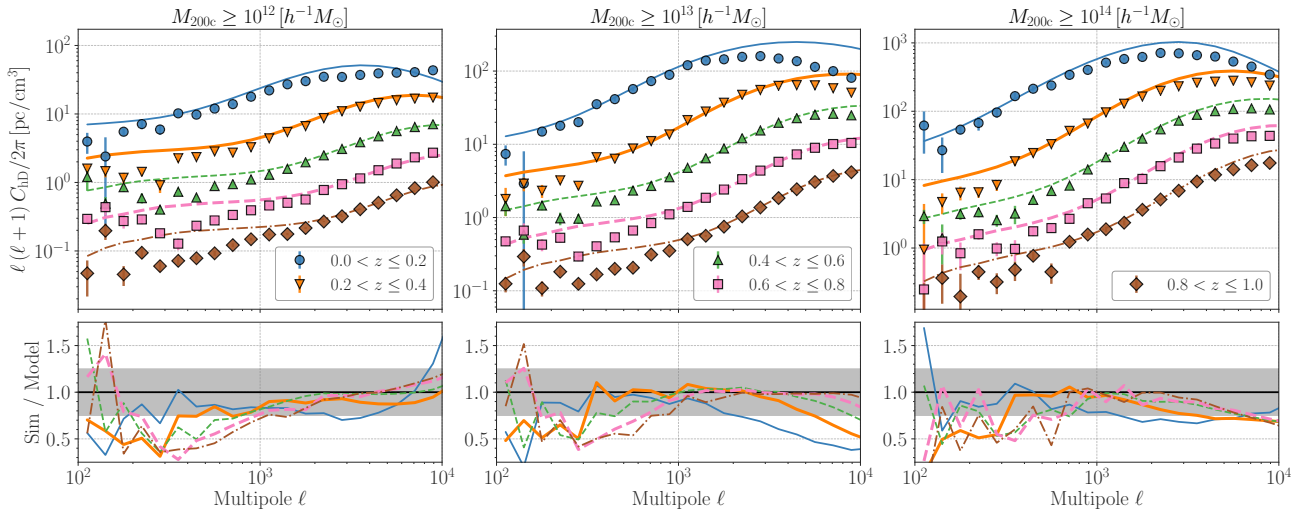


**Figure B1.** Comparison of the cross power spectra between haloes and DM in TNG simulations with our halo model. In each top panel, the different symbols show the power spectra at five redshift bins of  $0 < z \leq 0.2$ ,  $0.2 < z \leq 0.4$ ,  $0.4 < z \leq 0.6$ ,  $0.6 < z \leq 0.8$  and  $0.8 < z \leq 1.0$ ; the error bar is the standard deviation for the average over 27 realisations. The lines are our model predictions. From left to right, we show the comparison for haloes with their masses greater than  $10^{12}$ ,  $10^{13}$  and  $10^{14} h^{-1} M_{\odot}$ . To avoid any confusion, we multiply the power spectra at each redshift bin by  $10^0$ ,  $10^{-0.4}$ ,  $10^{-0.8}$ ,  $10^{-1.2}$  and  $10^{-1.6}$  from the lowest to highest redshift bins. In each bottom panel, we show the ratio of the power spectrum between the simulation results and halo-model counterparts. The grey shaded region in the bottom highlights  $\pm 25\%$ -level differences.

For a given halo sample, we construct the over density field in the halo number density on  $5400 \times 5400$  grids in a sky of  $6 \times 6 \text{ deg}^2$ . Note that the same angular grid is adopted in the DM maps. For a given set of DM map  $D(\theta)$  and halo over-density field  $\delta_{\text{h}}^{2\text{D}}(\theta)$ , we estimate the cross power spectrum as follows:

$$\hat{C}_{\text{hD}}(\ell) = \frac{1}{N_{\ell}} \sum_{\ell_i: |\ell_i| \leq \ell} \text{Re} \left[ \tilde{\delta}_{\text{h}}^{2\text{D}}(\ell) \tilde{D}^*(\ell) \right], \quad (\text{B1})$$

where the summation runs over modes whose lengths lie in the range  $\ell - \Delta\ell/2 \leq |\ell| \leq \ell + \Delta\ell/2$  for the assumed bin width  $\Delta\ell$ ,  $\tilde{\delta}_{\text{h}}^{2\text{D}}(\ell)$  is the Fourier counterpart of  $\delta_{\text{h}}^{2\text{D}}(\theta)$ ,  $\tilde{D}^*(\ell)$  is the complex conjugate of  $\tilde{D}(\ell)$  and  $\text{Re}[X]$  takes the real part of a given complex number  $X$ . In Eq. (B1),  $N_{\ell}$  represents the number of Fourier modes in a given bin of  $\ell$ . We set the width to  $\Delta \ln \ell = 0.23$  in the range of  $100 < \ell < 10^4$ .

Figure B1 summarises the comparison of our model of  $C_{\text{hD}}$  and the simulation results. For the simulation results, we show the average power spectrum over 27 realisations; the error bars represent the standard deviation divided by  $\sqrt{27}$ . For a visualisation purpose, we multiply the power spectra in the range of  $0 < z \leq 0.2$ ,  $0.2 < z \leq 0.4$ ,  $0.4 < z \leq 0.6$ ,  $0.6 < z \leq 0.8$  and  $0.8 < z \leq 1.0$  by  $10^0$ ,  $10^{-0.4}$ ,  $10^{-0.8}$ ,  $10^{-1.2}$  and  $10^{-1.6}$ , respectively. The figure illustrates that our model can provide a fit to the simulation results in a wide range of  $\ell$ , halo masses and redshifts. The model precision reaches about 25%; overall shapes of the power spectrum are well explained by our halo model. Our model relies on several fitting formulas of large-scale structures. We also summarised some action items to develop a more precise model of  $C_{\text{hD}}$  in Subsection 6.1.

## REFERENCES

Anderson M. E., Gaspari M., White S. D. M., Wang W., Dai X., 2015, *MNRAS*, **449**, 3806  
 Aricò G., Angulo R. E., Hernández-Monteaquedo C., Contreras S., Zennaro M., Pellejero-Ibañez M., Rosas-Guevara Y., 2020, *MNRAS*, **495**, 4800  
 Asgari M., et al., 2021, *A&A*, **645**, A104

Baby I. V., McNamara B. R., Nulsen P. E. J., Hogan M. T., Vantghem A. N., Russell H. R., Pulido F. A., Edge A. C., 2018, *ApJ*, **857**, 32  
 Bannister K. W., et al., 2019, *Science*, **365**, 565  
 Bassa C. G., et al., 2017, *ApJ*, **843**, L8  
 Battaglia N., Bond J. R., Pfrommer C., Sievers J. L., 2015, *ApJ*, **806**, 43  
 Behroozi P. S., Wechsler R. H., Conroy C., 2013, *ApJ*, **770**, 57  
 Behroozi P., Wechsler R. H., Hearin A. P., Conroy C., 2019, *MNRAS*, **488**, 3143  
 Beltz-Mohrmann G. D., Berlind A. A., 2021, arXiv e-prints, p. arXiv:2103.05076  
 Bennett C. L., et al., 2013, *ApJS*, **208**, 20  
 Berlind A. A., et al., 2003, *ApJ*, **593**, 1  
 Bhandari S., et al., 2020a, *ApJ*, **895**, L37  
 Bhandari S., et al., 2020b, *ApJ*, **901**, L20  
 Bhardwaj M., et al., 2021, *ApJ*, **910**, L18  
 Blandford R., Narayan R., 1985, *MNRAS*, **213**, 591  
 Bocquet S., Saro A., Dolag K., Mohr J. J., 2016, *MNRAS*, **456**, 2361  
 Bonamente M., Nevalainen J., Tilton E., Liivamägi J., Tempel E., Heinämäki P., Fang T., 2016, *MNRAS*, **457**, 4236  
 Bregman J. N., 2007, *ARA&A*, **45**, 221  
 CHIME/FRB Collaboration et al., 2018, *ApJ*, **863**, 48  
 CHIME/FRB Collaboration et al., 2020, *Nature*, **582**, 351  
 Cen R., Ostriker J. P., 1999, *ApJ*, **514**, 1  
 Chatterjee S., et al., 2017, *Nature*, **541**, 58  
 Chawla P., et al., 2021, arXiv e-prints, p. arXiv:2107.10858  
 Chisari N. E., et al., 2019, *The Open Journal of Astrophysics*, **2**, 4  
 Chittidi J. S., et al., 2020, arXiv e-prints, p. arXiv:2005.13158  
 Connor L., Ravi V., 2021, arXiv e-prints, p. arXiv:2107.13692  
 Connor L., Lin H.-H., Masui K., Oppermann N., Pen U.-L., Peterson J. B., Roman A., Sievers J., 2016, *MNRAS*, **460**, 1054  
 Cooke R. J., Pettini M., Steidel C. C., 2018, *ApJ*, **855**, 102  
 Cooray A., Sheth R., 2002, *Phys. Rep.*, **372**, 1  
 Cordes J. M., Chatterjee S., 2019, *ARA&A*, **57**, 417  
 Cordes J. M., Lazio T. J. W., 2002, arXiv e-prints, pp astro-ph/0207156  
 Cordes J. M., Ocker S. K., Chatterjee S., 2021, arXiv e-prints, p. arXiv:2108.01172  
 Crawford F., Kaspi V. M., Manchester R. N., Lyne A. G., Camilo F., D’Amico N., 2001, *ApJ*, **553**, 367  
 Cunha C. E., Huterer D., Busha M. T., Wechsler R. H., 2012, *MNRAS*, **423**,

- 909
- Davies J. J., Crain R. A., McCarthy I. G., Oppenheimer B. D., Schaye J., Schaller M., McAlpine S., 2019, *MNRAS*, **485**, 3783
- Deng W., Zhang B., 2014, *ApJ*, **783**, L35
- Diemer B., Kravtsov A. V., 2015, *ApJ*, **799**, 108
- Dubois Y., et al., 2014, *MNRAS*, **444**, 1453
- Duffy A. R., Schaye J., Kay S. T., Dalla Vecchia C., Battye R. A., Booth C. M., 2010, *MNRAS*, **405**, 2161
- Eisenstein D. J., Hu W., 1998, *ApJ*, **496**, 605
- Ford A. B., et al., 2016, *MNRAS*, **459**, 1745
- Fukugita M., Peebles P. J. E., 2004, *ApJ*, **616**, 643
- Fukugita M., Hogan C. J., Peebles P. J. E., 1998, *ApJ*, **503**, 518
- Giodini S., Lovisari L., Pointecouteau E., Ettori S., Reiprich T. H., Hoekstra H., 2013, *Space Sci. Rev.*, **177**, 247
- Greco J. P., Hill J. C., Spergel D. N., Battaglia N., 2015, *ApJ*, **808**, 151
- Green S. B., Aung H., Nagai D., van den Bosch F. C., 2020, *MNRAS*, **496**, 2743
- Hall A., 2021, *MNRAS*, **505**, 4935
- Hand N., et al., 2012, *Phys. Rev. Lett.*, **109**, 041101
- Hashimoto T., et al., 2020, *MNRAS*, **497**, 4107
- Heintz K. E., et al., 2020, *ApJ*, **903**, 152
- Hellwing W. A., Schaller M., Frenk C. S., Theuns T., Schaye J., Bower R. G., Crain R. A., 2016, *MNRAS*, **461**, L11
- Hernández-Monteagudo C., Ma Y.-Z., Kitaura F. S., Wang W., Génova-Santos R., Macías-Pérez J., Herranz D., 2015, *Phys. Rev. Lett.*, **115**, 191301
- Hikage C., Mandelbaum R., Takada M., Spergel D. N., 2013, *MNRAS*, **435**, 2345
- Hikage C., et al., 2019, *PASJ*, **71**, 43
- Hill J. C., Baxter E. J., Lidz A., Greco J. P., Jain B., 2018, *Phys. Rev. D*, **97**, 083501
- Hummels C. B., Bryan G. L., Smith B. D., Turk M. J., 2013, *MNRAS*, **430**, 1548
- Inoue S., 2004, *MNRAS*, **348**, 999
- Ioka K., 2003, *ApJ*, **598**, L79
- Jain B., Seljak U., 1997, *ApJ*, **484**, 560
- James C. W., Prochaska J. X., Macquart J. P., North-Hickey F., Bannister K. W., Dunning A., 2021, arXiv e-prints, p. arXiv:2101.07998
- Kilbinger M., 2015, *Reports on Progress in Physics*, **78**, 086901
- Kokubo M., et al., 2017, *ApJ*, **844**, 95
- Kravtsov A. V., Vikhlinin A. A., Meshcheryakov A. V., 2018, *Astronomy Letters*, **44**, 8
- Law C. J., et al., 2020, *ApJ*, **899**, 161
- Le Brun A. M. C., McCarthy I. G., Schaye J., Ponman T. J., 2014, *MNRAS*, **441**, 1270
- Leauthaud A., et al., 2010, *ApJ*, **709**, 97
- Lewis A., Challinor A., Lasenby A., 2000, *ApJ*, **538**, 473
- Li Z., Gao H., Wei J. J., Yang Y. P., Zhang B., Zhu Z. H., 2020, *MNRAS*, **496**, L28
- Lim S. H., Barnes D., Vogelsberger M., Mo H. J., Nelson D., Pillepich A., Dolag K., Marinacci F., 2021, *MNRAS*, **504**, 5131
- Lima M., Hu W., 2005, *Phys. Rev. D*, **72**, 043006
- Limber D. N., 1954, *ApJ*, **119**, 655
- Linder E. V., 2005, *Phys. Rev. D*, **72**, 043529
- Ludlow A. D., Navarro J. F., Angulo R. E., Boylan-Kolchin M., Springel V., Frenk C., White S. D. M., 2014, *MNRAS*, **441**, 378
- Macquart J. P., et al., 2020, *Nature*, **581**, 391
- Madhavacheril M. S., Battaglia N., Smith K. M., Sievers J. L., 2019, *Phys. Rev. D*, **100**, 103532
- Mandelbaum R., 2018, *ARA&A*, **56**, 393
- Mannings A. G., et al., 2020, arXiv e-prints, p. arXiv:2012.11617
- Marcote B., et al., 2020, *Nature*, **577**, 190
- Marinacci F., et al., 2018, *MNRAS*, **480**, 5113
- Mas-Ribas L., Hennawi J. F., 2018, *AJ*, **156**, 66
- McCarthy I. G., Schaye J., Bird S., Le Brun A. M. C., 2017, *MNRAS*, **465**, 2936
- McDonald M., et al., 2013, *ApJ*, **774**, 23
- McQuinn M., 2014, *ApJ*, **780**, L33
- McQuinn M., 2016, *ARA&A*, **54**, 313
- Mead A. J., Verde L., 2021, *MNRAS*, **503**, 3095
- Meinke J., Böckmann K., Cohen S., Maukopf P., Scannapieco E., Sarmento R., Lunde E., Cottle J., 2021, *ApJ*, **913**, 88
- Mo H. J., White S. D. M., 1996, *MNRAS*, **282**, 347
- Muñoz J. B., Kovetz E. D., Dai L., Kamionkowski M., 2016, *Phys. Rev. Lett.*, **117**, 091301
- Murata R., Nishimichi T., Takada M., Miyatake H., Shirasaki M., More S., Takahashi R., Osato K., 2018, *ApJ*, **854**, 120
- Nagai D., Lau E. T., 2011, *ApJ*, **731**, L10
- Naiman J. P., et al., 2018, *MNRAS*, **477**, 1206
- Navarro J. F., Frenk C. S., White S. D. M., 1996, *ApJ*, **462**, 563
- Nelson D., et al., 2018, *MNRAS*, **475**, 624
- Nicastro F., et al., 2018, *Nature*, **558**, 406
- Nuza S. E., et al., 2013, *MNRAS*, **432**, 743
- Osato K., Takada M., 2021, *Phys. Rev. D*, **103**, 063501
- Peebles P. J. E., Yu J. T., 1970, *ApJ*, **162**, 815
- Péroux C., Howk J. C., 2020, *ARA&A*, **58**, 363
- Petroff E., et al., 2017, arXiv e-prints, p. arXiv:1710.08155
- Pillepich A., et al., 2018, *MNRAS*, **475**, 648
- Planck Collaboration et al., 2016, *A&A*, **594**, A13
- Planck Collaboration et al., 2020, *A&A*, **641**, A6
- Prochaska J. X., et al., 2019, *Science*, **366**, 231
- Qiang D.-C., Wei H., 2021, *Phys. Rev. D*, **103**, 083536
- Rafiei-Ravandi M., Smith K. M., Masui K. W., 2020, *Phys. Rev. D*, **102**, 023528
- Rafiei-Ravandi M., et al., 2021, arXiv e-prints, p. arXiv:2106.04354
- Ravi V., et al., 2019, *Nature*, **572**, 352
- Riess A. G., 2020, *Nature Reviews Physics*, **2**, 10
- Sato M., Hamana T., Takahashi R., Takada M., Yoshida N., Matsubara T., Sugiyama N., 2009, *ApJ*, **701**, 945
- Schaan E., et al., 2016, *Phys. Rev. D*, **93**, 082002
- Schaan E., et al., 2021, *Phys. Rev. D*, **103**, 063513
- Schaye J., et al., 2015, *MNRAS*, **446**, 521
- Schneider A., Teyssier R., 2015, *J. Cosmology Astropart. Phys.*, **2015**, 049
- Secco L. F., et al., 2021, arXiv e-prints, p. arXiv:2105.13544
- Sheth R. K., Tormen G., 1999, *MNRAS*, **308**, 119
- Shirasaki M., Kashiyama K., Yoshida N., 2017, *Phys. Rev. D*, **95**, 083012
- Simha S., et al., 2020, *ApJ*, **901**, 134
- Singh P., Majumdar S., Nath B. B., Silk J., 2018, *MNRAS*, **478**, 2909
- Spitler L. G., et al., 2016, *Nature*, **531**, 202
- Springel V., 2010, *MNRAS*, **401**, 791
- Springel V., et al., 2018, *MNRAS*, **475**, 676
- Sugiyama N. S., Okumura T., Spergel D. N., 2018, *MNRAS*, **475**, 3764
- Sunyaev R. A., Zeldovich Y. B., 1970, *Ap&SS*, **7**, 3
- Sunyaev R. A., Zeldovich Y. B., 1980, *MNRAS*, **190**, 413
- Takada M., Hu W., 2013, *Phys. Rev. D*, **87**, 123504
- Takahashi R., Ioka K., Mori A., Funahashi K., 2021, *MNRAS*, **502**, 2615
- Taylor J. H., Cordes J. M., 1993, *ApJ*, **411**, 674
- Tendulkar S. P., et al., 2017, *ApJ*, **834**, L7
- The CHIME/FRB Collaboration et al., 2021, arXiv e-prints, p. arXiv:2106.04352
- Tinker J., Kravtsov A. V., Klypin A., Abazajian K., Warren M., Yepes G., Gottlöber S., Holz D. E., 2008, *ApJ*, **688**, 709
- Tinker J. L., Robertson B. E., Kravtsov A. V., Klypin A., Warren M. S., Yepes G., Gottlöber S., 2010, *ApJ*, **724**, 878
- Tumlinson J., Peebles M. S., Werk J. K., 2017, *ARA&A*, **55**, 389
- Vazza F., Eckert D., Simionescu A., Brüggén M., Ettori S., 2013, *MNRAS*, **429**, 799
- Vikram V., Lidz A., Jain B., 2017, *MNRAS*, **467**, 2315
- Wechsler R. H., Tinker J. L., 2018, *ARA&A*, **56**, 435
- Weinberg D. H., Mortonson M. J., Eisenstein D. J., Hirata C., Riess A. G., Rozo E., 2013, *Phys. Rep.*, **530**, 87
- Wu X., Mo H., Li C., Lim S., 2020, *ApJ*, **903**, 26
- Wu Q., Zhang G. Q., Wang F. Y., 2021, arXiv e-prints, p. arXiv:2108.00581
- Yao J. M., Manchester R. N., Wang N., 2017, *ApJ*, **835**, 29
- Zu Y., Mandelbaum R., 2015, *MNRAS*, **454**, 1161
- van Daalen M. P., McCarthy I. G., Schaye J., 2020, *MNRAS*, **491**, 2424
- van de Voort F., Schaye J., 2012, *MNRAS*, **423**, 2991

van de Voort F., Quataert E., Hopkins P. F., Faucher-Giguère C.-A., Feldmann R., Kereš D., Chan T. K., Hafen Z., 2016, *MNRAS*, **463**, 4533

This paper has been typeset from a  $\text{\TeX}/\text{\LaTeX}$  file prepared by the author.